Structural Durability & Health Monitoring

Tech Science Press

https://doi.org/10.32604/sdhm.2026.077081

ARTICLE

Punching in Fiber-Reinforced, Net-Reinforced, and Unreinforced Concrete Slabs under Static, Impulsive, and Thermal Loading

Roberto Felicetti, Pietro G. Gambarova* and Francesco Lo Monte

Department of Civil and Environmental Engineering, Politecnico di Milano, Milan, Italy

*Corresponding Author: Pietro G. Gambarova. Email: pietro.gambarova@polimi.it

Received: 02 December 2025; Accepted: 31 March 2026; Published: 18 May 2026

ABSTRACT: Many tests have been conducted over the years in Milan on moderately-thick concrete slabs—with diameter-to-thickness ratios of 5 and 5.5—either reinforced or unreinforced, all subjected to punching, with different mixes, reinforcement technologies, and loading procedures. Their results are revisited systematically in this paper, starting from a thorough review of the literature on moderately thick concrete slabs. The specimens were either square (but fastened to a circular support) or circular. In three experimental campaigns, 99 specimens were tested: 50 under quasi-static loading (including 16 exposed to high temperatures) and 49 under impulsive loading. The first campaign investigated concrete slabs reinforced with polyacrylonitrile fibers, steel fibers, or steel nets, focusing on their deformed shapes and failure modes under quasi-static punching. The second campaign examined the effects of high temperatures on unreinforced and net-reinforced slabs subjected to quasi-static punching, while the third campaign focused on the failure modes and energy issues of fiber-reinforced slabs under impulsive punching. Polyacrylonitrile fibers increase punching resistance under impact, but change the failure mode from mixed (bending + punching) to pure punching. Steel nets increase slab ductility more than steel fibers, while high temperatures promote a shift from bending-controlled to shear-controlled failure modes. The main contributions of the test results are: (a) the varying degree of softening in the slab's response to punching due to the formation of either small or large punching cones; (b) the reduction in bearing capacity with increasing temperature, which occurs more in net-reinforced than in fiber-reinforced slabs; and (c) the different contributions to the total dissipated energy under impact, resulting from the formation of bending-related cracks and of the punching cone. Overall, this work aims to highlight general trends in slab behavior under punching loads in different conditions, using highly idealized tests (as often done in labs), that provide a basic representation of actual punching scenarios.

KEYWORDS: Concrete slabs; steel nets; polymeric/steel fibers; static/impulsive punching; high temperatures; failure modes; energy balance (in slab punching)

1 Introduction and State-of-the Art Literature

The subject of *punching shear*—or simply *punching*—in reinforced-concrete slabs and plates has long fascinated scholars and designers throughout the century-old history of reinforced concrete (RC). In fact, in addition to the many papers published in the latter half of the twentieth century (CEB, 1985 [1]; *fib*, 2001 [2]), hundreds of studies have addressed this issue since the beginning of the new millennium. They appear in leading journals, major conferences and congresses, widely circulated technical reports, and both national and international design codes (see the review by Venkata Ramana, 2017 [3]). There are at least three reasons for this widespread interest. The first relates to the complex bending- or shear-controlled behavior, or even mixed behavior of slabs and plates, along with the resulting crack patterns and the failure modes, depending on whether shear and bending reinforcement or fibers are provided. The second reason is the variety of situations in which punching shear governs structural behavior, ranging from thin slabs supported by columns to moderately thick slabs subjected to the highly concentrated loads transmitted by the supports of heavy machinery or by compact flying objects (*missiles*). The third reason is the introduction of new materials like high- and ultra high-performance concretes (HPCs and UHPCs), as a replacement or supplement of normal-strength concrete (NSC).

The design requirements and research objectives concerning the punching of structural concrete slabs were first addressed systematically in CEB Bulletin 168 (1985) [1], where the focus was on several key issues, including the description of the punching behavior in RC slabs, lower-bound solutions for evaluating the bearing capacity in punching, comparisons between the design provisions of several codes and test results, the mechanical properties of steel fiber-reinforced concrete, and fatigue in concrete. Numerous studies and additional tests were later performed to examine the behavior of slabs made of high-performance concrete, as well as the role of different fibers under static punching, even at high temperatures (see refs. in Felicetti et al., 1995 [4]; Felicetti and Gambarova, 2000 [5]; Guastini et al., 2013 [6]). Investigations have also considered impact punching (Gambarova and Schumm, 1994 [7]).

With the advent of the new millennium, however, other topics emerged. Several key issues were addressed in *fib* Bulletin 12 (2001) [2], including the size effect in the punching failure of shear-unreinforced slabs, strut-and tie systems in shear-reinforced slabs, mixed failure modes (resulting from bending and punching), specialized shear-reinforcing systems (such as stud rails and double-headed studs), and the relationship between structural behavior and testing.

In *fib* Bulletin 57 (2010) [8], particular attention was devoted to the modelling of fiber-reinforced slabs and their failure in punching, especially in column-slab connections. Steel fibers as a substitute for minimum reinforcement were also investigated, and code provisions concerning punching were reviewed.

The subsequent publications on punching, such as *fib* Bulletin 81 and ACI SP 315, 2017 [9] by Ospina et al., mainly focused on column-slab connections, including edge connections. Other topics were size effect in concrete slabs with or without shear reinforcement, models based on the Critical Shear-Crack Theory, flexure-induced punching under monotonic or cyclic loading, one-way vs. two-way flat slabs, post-punching response, and the robustness of concrete flat slabs.

Punching in concrete slabs leads to different failure modes (Fig. 1) depending on whether a mixed-mode behavior with both bending and shear or a shear-type behavior—with the formation of a punching cone—prevails (Walraven et al., 1993 [10]).

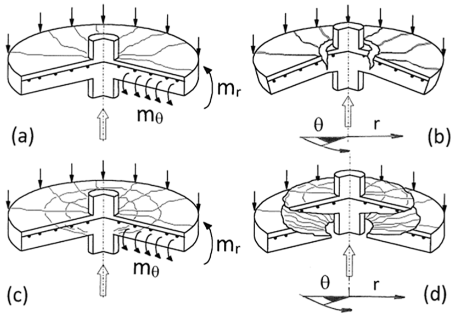

Figure 1: Slab failure modes: (**a**) by bending; (**b**) by bending and shear; (**c**) by punching-induced shear with some bending; and (**d**) by punching-induced shear.

Focusing on solid, unreinforced or fiber-/net-reinforced slabs made of ordinary, high-performance and ultra high-performance concrete, notable test results include those by Zamri et al. (2022) [11] and Liu et al. (2025) [12], who investigated the introduction of steel fibers, while Sucharda et al. (2018) [13], Bassurucu et al. (2023) [14] and Hernández Fraile et al. (2024) [15] examined the effect that bars, stirrups and studs may have on the shape of the punching cone and on the behavior of RC slabs on the ground, as well as the effect of steel-fiber alignment and distribution.

Shear-type behavior is typical of relatively thick concrete slabs and, in general, of regions closest to the punching force (within the contraflexure *hogging* zone for downward loads and upward reactions). Further insights into punching as a localized event, characterized by the interaction between shear-induced and bending-induced cracking, are provided in the papers by Nguyen-Minh et al. (2011) [16] on how steel fibers may limit concrete damage, Mabrouk and Hegab (2017) [17] on the role of reinforcement ratios (bars and stirrups), Bentz and Netopilik (2013) [18] on size effect, and Trekin and Pekin (2019) [19] on full-scale column-slab connections. With regard to this issue, De Sousa et al. (2020) [20] tested one-way slabs to examine the transition from global failure modes, caused by one-way shear and bending, to localized shear-related failure modes, a topic addressed in both static and dynamic conditions in two sections of this work.

The complex 3D aspects of punching and the many parameters involved are the subject of in-depth studies by Marí et al. (2023) [21] (who examined and modelled the differences between beams and slabs subjected to punching), Said et al. (2020) [22], Schmidt et al. (2020) [23], Bashandy et al. (2022) [24], and Awad et al. (2024) [25]. These authors examined, from different perspectives, the various technologies based on standard shear reinforcement and special shear-resisting devices, as well as their replacement or supplementation with steel fibers, an issue treated also in the first and third parts of this study.

The intriguing issue of enhancing the mechanical properties of the punching region was addressed by Hamoda et al. (2025) [26]. In their tests, the punching shear zone was filled with high-performance and ultra high-performance concrete to improve the cracking behavior, ultimate bearing capacity, elastic stiffness, failure modes, crack patterns, and energy-absorption capability. Crack patterns and failure modes are also discussed in the first section of this paper, where more details and quantitative indications are provided on the contributions of bending-induced cracks and punching-cone formation.

Extreme environmental and loading conditions, such as fire and impact, have also attracted considerable attention from several scholars since the pioneering studies on fire by Kordina and on impact loading by Banthia, Bentur, and Mindess (see the review by Daud et al., 2025 [27]) in the second half of the previous century.

With reference to fire, and more generally to high temperatures, several studies under sustained loading can be cited: Bamonte et al. (2009, 2012) [28,29] investigated the roles of concrete mechanical decay and indirect actions in punching failure of slabs, as well as the reliability of the Critical Shear-Crack Theory applied to RC slabs exposed to fire; Ghoreishi et al. (2013, 2015) [30,31] examined the capacity and cracking behavior of relatively thin transversely-unreinforced RC slabs both after cooling and during exposure to high temperatures (close to 300°C); Annerel et al. (2013) [32] studied real-scale reinforced square slabs with and without stirrups; Smith (2016) [33] focused on laterally-restrained slabs, with and without shear reinforcement, for various reinforcement ratios and thicknesses. Finally, Ožbolt et al. (2019) [34] investigated RC slabs damaged by fire and subsequently subjected to impact loading. The loss of bearing capacity, as well as the evolution of crack patterns and failure modes with temperature, is also addressed in the second section of this paper, for both plain-concrete and net-reinforced slabs.

With reference to slab punching under dynamic conditions (impact loading), the astonishing volume of research conducted over the past ten-to-fifteen years, as cited by Daud et al. (2025) [27], shows that issues such as boundary conditions, scaling (specimens vs. real structures), concrete strain-rate sensitivity, energy dissipation, shear-vs.-bending-type failure, reinforcement arrangement, fibers, membrane behavior, and failure modes remain active topics. Some of these—shear-vs.-bending-type failure, energy dissipation, the role of fiber, and failure modes—are addressed in the experiments and discussions presented in the third section of this paper.

The extensive database obtained from these tests has been complemented by the development of analytical and numerical models to describe punching mechanisms, accounting for the many parameters involved, as well as by design-oriented equations and expressions for evaluating the ultimate punching capacity. Among the models, those proposed by Hoang and Pop (2015) [35] and by Biyan et al. (2023) [36] are noteworthy. Hoang and Pop developed a model based on the upper-bound theorem of the theory of plasticity, incorporating a mechanism that includes circumferential and radial cracks (the *Crack Sliding Model*), a topic discussed extensively in the first and third sections of this paper. Biyan et al. studied the behavior of square RC slabs subjected to shear punching with varying side-to-thickness ratios (from 4.5 to 10) using numerical simulations. Their results provide valuable information on relatively thick slabs, such as those examined in this study (side-to-thickness ratio = 5.0–5.5).

Among the contributions to slab design, the comprehensive work by Huang et al. (2016) [37] and dos Santos et al. (2022) [38] on the validity of various design equations for NSC and HSC slabs—considering size effect, critical perimeter, and corner slab-column connections—should be highlighted, as well as the many tests performed in Lausanne (at EPFL) by Muttoni and coworkers. These tests are the basis of the Critical Shear-Crack Theory (Muttoni and Fernández Ruiz, 2010 [39]) recently adopted by the Eurocode EC 2 (2023) [40]. The size effect in the punching of reinforced and unreinforced slabs deserves special attention. Dönmez and Bažant (2017) [41] demonstrated its importance for updating ACI 318's equation for punching bearing capacity. However, for slab thicknesses below 100 mm, as in the slabs tested in the following sections, the size effect plays a minor role. All these papers address the *hogging regions* around slab-column connections, as also considered in the following sections, which summarize the numerous test results obtained in Milan on moderately thick concrete slabs representing the *hogging region* around a loaded area, where localized forces—either static or impulsive—are applied.

2 Objectives, Specimen Geometry, and Test Classification

The main objectives of the three experimental campaigns presented in this paper are as follows:

- Test Series A (Fig. 2a): Polyacrylonitrile fiber-, steel fiber-, and steel net-reinforced slabs subjected to static punching, focusing on load-displacement responses for different fiber or steel content, deformed shapes, collapse modes, and cracking;
- Test Series B (Figs. 2b and 3a,b): Net-reinforced and plain-concrete slabs subjected to static punching, exposed to high temperatures, with attention to peak load, deformed shape, truncated-cone profile, and bending- and punching-induced displacements ($T \leq 400^\circ$C);
- Test Series C (Fig. 2a): Concrete slabs reinforced with polyacrylonitrile fibers, subjected to static and impulsive loading, with analysis of collapse modes, energy balance, bending-punching interaction, and truncated-cone formation.

The specimens—either square (Fig. 2a) or circular (Fig. 2b)—were partially-clamped along the boundary using 8 clamping levers for Test Series A and C, or 10 for Test Series B (Fig. 3a), acting on circular *clamping* or *restraining rings*.

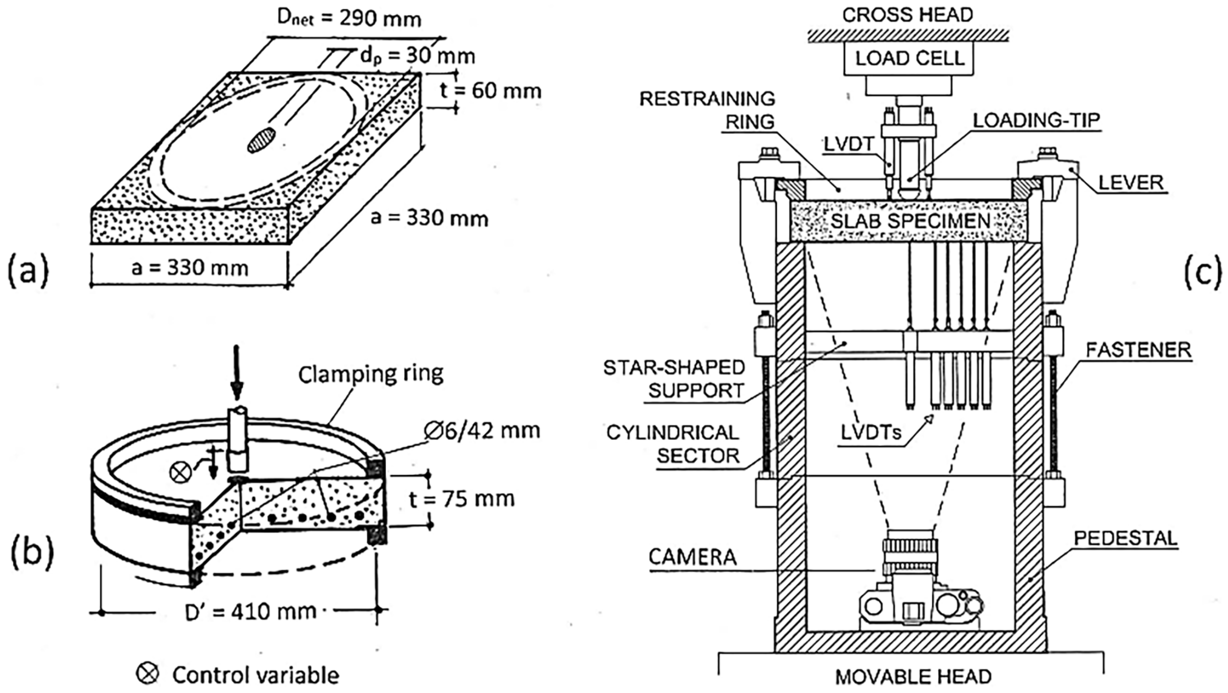

Figure 2: Specimen geometry and test setup: (**a**) Test Series A and C; (**b**) Test Series B; and (**c**) loading setup.

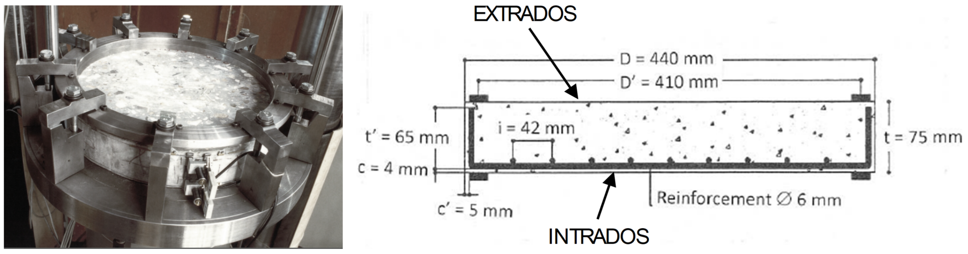

(a) (b)

Figure 3: Test Series B: (**a**) specimen blocked by ten levers and a clamping ring; and (**b**) reinforcement with a steel net; Specimens B0-N45-H.

The in-plan size of the specimens was chosen to allow the formation of a truncated punching cone with a slope α (Fig. 4a) smaller than 30°. Specifically, α_{min} = 21° in Tests Series B (nominal diameter of the support D' = 410 mm, thickness t = 75 mm, Fig. 2b), and α_{min} = 24° in Test Series A and C (nominal diameter of the circular support D_{net} = 290 mm, thickness 60 mm).

The nominal area enclosed by the circular support can be considered similar to the *hogging region* of a column supporting a circular slab (diameter D^*) clamped along its boundary and bearing downward loads. Since the diameter of the hogging region is approximately one-third of the clamped boundary diameter (Timoshenko and Woinowsky-Krieger, 1987 [42]), the specimens tested in this work represent the hogging region of a clamped circular slab with a diameter D^* roughly between 0.9 and 1.2 m, or with a diameter-to-thickness ratio (D^*/t) close to 15.

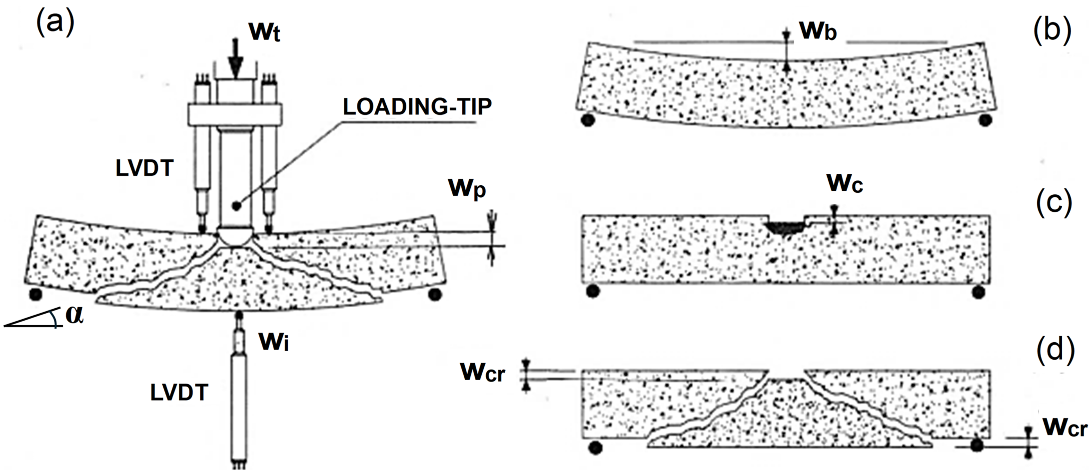

Figure 4: Sketch of the loading-tip instrumentation and symbols of the displacements: (**a**) deformed shape; (**b**) bending; (**c**) local crushing; and (**d**) formation and detachment of the punching cone.

It should be noted that under a punching load applied at the center of an elastic slab, square slabs—either simply-supported or built-in along the sides—behave very similarly to circular slabs in terms of maximum deflection in the center (Timoshenko and Woinowsky-Krieger, 1987 [42]). This is even more pronounced when the support of a square slab is along the circle enveloped by the sides, as in Test Series A and C. Consequently, the different geometries of the specimens belonging to the three series have been neglected.

Each specimen has an 8-character alpha-numeric label for identification (Appendix A):

$$XT - Yfdl - Zq$$

where:

- X = A for Test Series A; = B for Test Series B; = C for Test Series C;
- T = 0 for the tests at ambient temperature (T = 20°C); = 1, 2, 3 for the tests in residual conditions (T_{max} = 105°C, 250°C, 400°C);
- Y = C for plain concrete; = P for PAN fibers; = S for steel fibers; = N for steel net;
- Z = N for NSC ($f_c < 60$ MPa); = H for HPC ($f_c \geq 60$ MPa);
- f = 1–4 for fiber or reinforcement content by volume (v_f = 0.5, 1.0, 1.5, 2%), see Appendix B;
- d = 1–5 for fiber or bar diameter (d_f = 30, 100, 500 μm for fibers; d_s = 5, 6 mm for bars);
- l = 1–3 for fiber length (l_f = 12, 24, 36 mm for PAN fibers or 30 mm for steel fibers); omitted for steel bars; in general, f, d, and l are omitted if not required by identification;
- $q \leq 3$ for the nominally-identical specimens tested in each sub-case of Test Series A ($q \leq 2$), B ($q = 2$), and C ($q \leq 3$); omitted whenever (a) the average value is reported, or (b) the information has no specific relevance (Appendix C).

3 Materials Properties, Reinforcement, and Number of the Specimens

In the three experimental campaigns, two concrete mixes were used, a medium-grade blended cement (42.5R-II/A-LL) suitable for a normal-strength concrete, and a high-grade Portland cement (52.5R-I) suitable for a high-performance concrete (see Table 1).

All mixes are fairly *lean*, as the cement content barely exceeds 300 kg/m^3. The better properties at room temperature of the mix adopted in Test Series B were justified by the need to enhance the role of high-temperature, as HPCs are (slightly) more heat-sensitive than NSCs.

Table 1: Concrete mix design and strength, reinforcement, and test temperature.

Test Series **Specimens**	**A—Fig. 2a** **A0-C/P/S/N-N**	**B—Fig. 2b** **B0/1/2/3-C/N-H**	**C—Fig. 2a** **C0-C/P-N**
Specimen's shape and size	Square, 330 mm × 60 mm	Circular, 440 mm × 75 mm	Square, 330 mm × 60 mm
Temperature (T) [C°]	20	20, 105, 250, 400	20
No. of specimens	22* + 4ˆ + 4# + 4§	8# + 8§	49
Cement type	Blended 42.5R-II/A-LL	Portland 42.5R-I	Blended 42.5R-II/A-LL
Cement content (c) [kg/m^3]	325	290 (+10.3% sf)	325
Sand+gravel [kg/m^3]	1770	1870	1770
Calcareous filler [kg/m^3]	130	105	130
Max. aggregate size (d_a) [mm]	$15^{\wedge\#\S}$; 25*	15	25
Effective water (w/b) [kg/m^3]	162 (0.50)	138 (0.43)	162 (0.50)
Fiber type/density [kg/m^3]	DRAMIX/7800; PAN/1200	–	PAN/1200
Steel yielding strength f_y [MPa]	320 hot-rolled	320 hot-rolled	–
Acrylic superplasticizer (sp/b)	1%	–	1%
Melammino-sulfonate sp (sp/b)	–	3.3%	–
Retarder (r_t/b)	–	0.5%	–
Density [kg/m^3]	2300–2400	2300	2300–2400
Target compr. strength f_{cN} [MPa]	40–45	70–75	40–45
Actual avg strength f_c [MPa]	$43^{\wedge\#\S}$, 46*	72	46

Note: (*) specimens with PAN fibers, same fiber content and properties in Test Series A and C; (ˆ) specimens with DRAMIX fibers; ($^\#$) (§) specimens reinforced with a two-way steel net and specimens made of plain concrete; sf = silica fume; b = binder = cement + silica fume or fly ash; sp = superplasticizer.

The larger aggregate size adopted in Test Series C (d_a = 25 mm compared to 15 mm in Test Series A and B) was justified by the need to obtain tougher concrete under dynamic punching.

Similar specimens—but with a higher steel ratio (= 2.0%–2.5% in two directions), a larger punching tip (d_p = t), and smaller aggregates (d_a = 6.35 mm)—were tested by Bažant and Cao (1987) [43] to investigate size effects (D = 250 and 500 mm, D/t = 5 in Groups I, II, and III, Sizes B and C).

4 Fiber-Reinforced and Net-Reinforced Square Slabs Subjected to Quasi-Static Punching—Test Series A

4.1 Geometry of the Specimens, Parameters under Investigation, and Number of the Tests

Laboratory tests on concrete-slab punching are notably subject to numerous constraints related to the geometry and capacity of the loading machine, as well as to the maximum aggregate size of the concrete, the fiber length, and the diameter of the reinforcing bars. A further constraint is associated with the sensitivity of the specimens to snap-back phenomena, which may occur during the softening phase due to the unstable propagation of through-cracks.

Other constraints may come from specific devices like the geometry of the oven or furnace used to heat the specimens, as in Test Series B, where the high-temperature chamber is 500 mm wide, 700 mm long, and 350 mm deep. Hence, the 34 square slabs tested in Test Series A have the dimensions indicated in Fig. 2a and are divided into 5 sub-series (see Appendix A).

4.2 Test Set-up, Instrumentation, and Displacements

All specimens were clamped to a cylindrical body (*cylindrical sector* in Fig. 2c), which was attached to the movable head of an Instron press (Type 8562), equipped with an electromechanical actuator (100 kN capacity). The punching tip was secured to the fixed head (=*cross head* in Fig. 2c), and the displacement was applied through the movable head supporting the pedestal.

All tests were displacement-controlled (w_t = 1 μm/s up to and beyond the peak load in the steepest part of the softening branch, and 4 μm/s thereafter, see Fig. 4a). The punching tip was fitted with 3 LVD transformers (max. displacement ± 5.0 mm). Two of the LVDTs are shown in Fig. 4a, where, for clarity, the specimen support is assumed to be fixed and the loading/punching tip movable. The three LVDTs measure the penetration of the tip $\mathrm{w_p}$ (Fig. 4a) resulting from the local crushing of the concrete beneath the loading tip (w_c, Fig. 4c) and the opening of the punching-shear crack (w_{cr}, Fig. 4d). It should be noted that these displacements (and the other displacements introduced in the following sections) are accompanied by slab bending (w_b, Fig. 4b) and their definitions are given below:

- w_t = displacement of the punching tip controlled by the press (given/enforced) = $w_b + w_c + w_{cr}$
- w_i = displacement at the intrados (measured)
- w_p = penetration of the punching tip (measured) = relative displacement between the loading tip and the undisturbed extrados (i.e., subjected only to the bending-induced deformation) = $w_c + w_{cr} = w_t - w_b$; the value of w_p is provided by the LVDTs fastened to the loading tip (Fig. 4a)
- w_c = penetration of the loading tip due to local concrete crushing = $w_t - w_i$
- w_{cr} = penetration of the loading tip due to the formation of the truncated cone = $w_p - w_c$
- w_b = displacement in the central part of the intrados caused by bending = $w_t - (w_c + w_{cr})$
- w_e = displacement at the extrados (not including the detachment of the truncated cone) = $w_b + w_c$

In 27 tests, the displacements at the intrados were measured using 16 LVDTs held in position by a specially-designed star-shaped support (Fig. 5a), which was fastened to the internal wall of the cylindrical body (Fig. 2c).

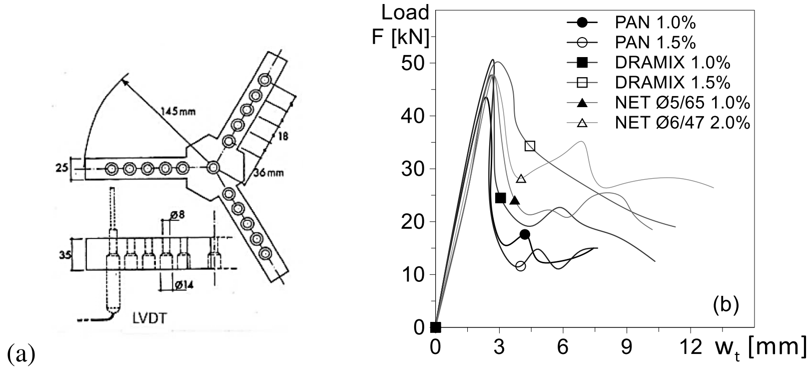

Figure 5: Star-shaped support carrying 16 LVDTs for measuring the displacement w_i at the intrados (**a**); and typical average load-displacement curves resulting from the tests A0-P/S/N-N (**b**).

This allowed the displacement w_i to be measured in the centroid of each specimen, as well as along three radial directions, at each step of the displacement-controlled loading process. In 7 tests, the star-shaped support and its instruments were removed to make room for a camera (Fig. 2c), which recorded the crack patterns at the intrados and made it possible to correlate singularities in the load-displacement curves with crack formation and propagation.

In Fig. 5b only the six most regular curves are plotted since test repeatability was more than satisfactory. The very similar specimens A0-P221-N and A0-P321-N (PAN fibers, v_f = 1% and 1.5%, symbols • and o, respectively) exhibit very close load-displacement curves, which is an indication of satisfactory test repeatability and reliability (For further discussion on test reliability, see Appendix C). A similar behavior is observed for specimens A0-N24-N and A0-N45-N (steel net, v_f = 1% and 2%, symbols ▲ and △, respectively), and A0-S233-N and A0-S333-N (DRAMIX fibers, v_f = 1% and 1.5%, symbols ■ and □, respectively). The response of these specimens, however, differs in an advanced stage of the softening phase, which is highly sensitive to fiber content.

4.3 Results

Role of reinforcement amount and type

Since the tests on PAN fiber-reinforced slabs indicate that the fiber aspect ratio $\lambda_f = l_f/d_f$ has a negligible effect on slab behavior, the discussion is limited to the content and type of reinforcement (Fig. 5b; PAN fibers: diameter, length, and aspect ratio: 100 μm, 12 mm, 120).

As expected, the initial extended, almost linear loading branch and the peak load are minimally affected by the reinforcement, while the residual strength in the post-peak phase is markedly higher using metallic reinforcement (steel net with v_f = 1% and 2%; DRAMIX fibers with v_f = 1% and 1.5%). Steel bars and fibers guarantee, therefore, a higher ductility compared to polymeric fibers.

In the two cases with the steel net (v_f = 1% and 2%), the post-peak part of the softening branch is as steep as in the cases with either polymeric or steel fibers. This indicates that the net—although more effective at large displacements—has a delayed response in resisting crack opening immediately after the peak load.

Failure modes

As a rule, the peak load was accompanied by the formation of a few radial cracks at the intrados, with an almost linear distribution of displacement in the radial direction for all loads below the peak load (Fig. 6a,b for two specimens containing PAN fibers).

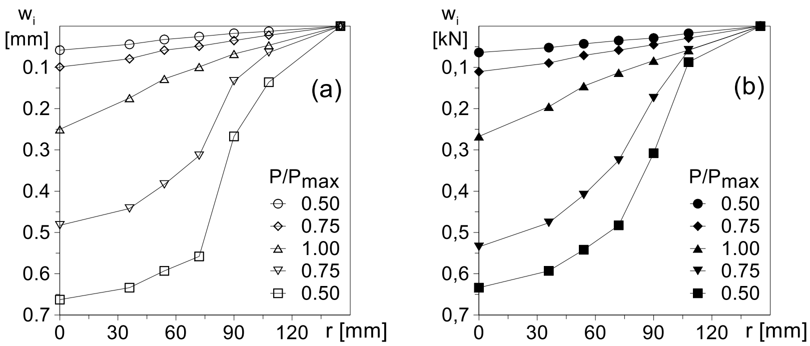

Figure 6: Radial diagrams of the deflection w_i measured along the intrados for various load levels: (**a**) Test A0-P-221-N1 with v_f = 1%; and (**b**) Test A0-P-321-N2 with v_f = 2%; PAN fibers in both cases; the diagrams are the average of the deflections measured in three radial directions at 120° (Fig. 5a); *r* is the radial coordinate of the circular domain enveloped by the restraining ring.

Beyond the peak load, during the softening phase, the displacement profiles become increasingly nonlinear and tend to flatten in the central region. While the pre-peak, mostly linear distribution of the displacement results primarily from the bending behavior accompanied by the formation of radial microcracks at the intrados (as in Case I, left-hand insert in Fig. 7a), the post-peak nonlinear distribution, with an almost *flat* central region, is a clear indication of the progressive formation of a truncated punching-shear cone. This cone tends to behave like a rigid body (as in Case II, right-hand insert in Fig. 7a). Furthermore, the higher the fiber or reinforcement content, the milder the transition from radial cracking to punching-shear cracking (Fig. 6a,b).

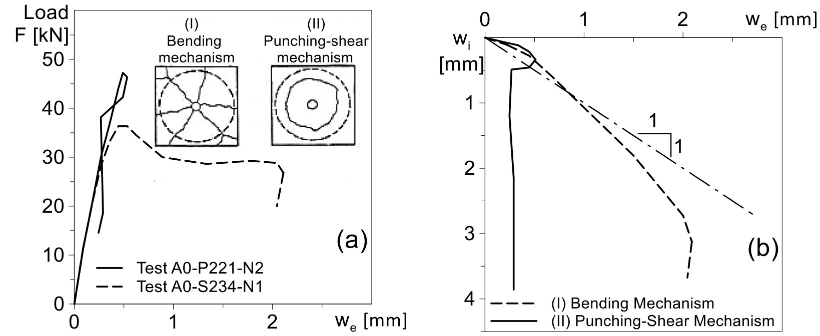

Figure 7: Typical deflection curves: (**a**) the load vs. the deflection w_e in the center of the extrados; and (**b**) deflection at the intrados w_i vs. the deflection at the extrados w_e; Test A0-S234-N1 (dash curves, DRAMIX fibers, bending-type failure), and Test A0-P221-N2 (full curves, PAN fibers, shear-type failure); $v_f = 1\%$.

As shown by Test A0-S234-N1 in Fig. 7 (dash curves, Case I, DRAMIX fibers), bending-type behaviors exhibit no *snap-back* (Fig. 7a), and the displacements at the extrados w_e and intrados w_i are very close and almost linearly related (Fig. 7b). In perfectly-elastic slabs, these displacements would be equal, provided that the normal strain in the vertical direction is negligible (as is the case in thin and moderately thick slabs). The closeness of the two displacements is a clear indication that the formation of the punching cone is deferred. On the contrary, as shown by Test A0-P221-N2 in Fig. 7a (solid curves, Case II, PAN fibers), punching shear-type behaviors are characterized by a *snap-back* of the displacement at the extrados w_e and an increasing displacement at the intrados w_i (Fig. 7b), which is a clear indication of the downward displacement of the punching-shear cone.

In general, few and thin radial cracks develop before and up to the load peak (Fig. 8a,b). In the softening phase, however, some radial cracks partially close, and some propagate (Fig. 8c,d). In the meantime, circumferential cracks form, clearly indicating the development of a truncated cone (Fig. 8e), until the eventual expulsion of the cone itself (Fig. 8f).

Depending on the reinforcement and the type of test—quasi-static tests under ordinary or residual conditions (Section 5), or impact tests (Section 6), *mixed crack patterns* may form, with radial and circumferential cracks coexisting at the intrados, and truncated cones of varying extent. Similar behaviors were also observed for PAN-fiber and steel-net reinforcement (see Appendix B). In the case of PAN fibers, the post-peak strength loss is more pronounced and the final sub-horizontal branch is shorter. For steel-net reinforcement, the strength loss is less pronounced, and the sub-horizontal branch is more extended.

It is noteworthy that the strength loss past the peak load is due to the progressive formation of the truncated cone, whose full extension—possibly related to the occurrence of other resistant mechanisms, such as membrane action—requires the dissipation of a sizable amount of energy, as indicated by the varying lengths of the horizontal branches beyond the softening phase and the formation of the punching cone (Fig. 8a). In this project, the residual strength after the cone formation was approximately 55%–60% of the peak load in specimens reinforced with a steel net, 30%–40% in the specimens reinforced with DRAMIX fibers, 15%–20% in those containing PAN fibers, and less than 20% in plain-concrete specimens. PAN-reinforced and plain-concrete specimens behaved similarly.

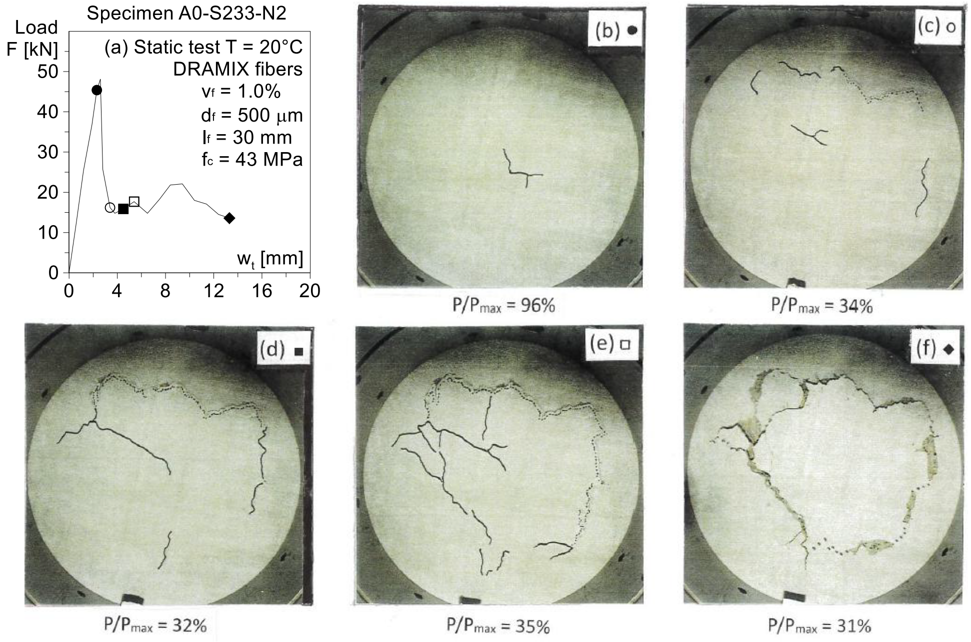

P/P_{max} = 96%

P/P_{max} = 34%

P/P_{max} = 32%

P/P_{max} = 35%

P/P_{max} = 31%

Figure 8: Quasi-static punching—DRAMIX fibers—Typical evolution of the crack pattern (Test A0-S233-N2): (**a**) load vs. loading-tip displacement curve; (**b**) first bending-controlled microcracks; (**c**,**d**) from radial to circumferential shear-controlled cracking; (**e**) development of the truncated cone, and (**f**) detachment of the truncated cone.

5 Fiber-Reinforced Circular Slabs Subjected to Static Punching past a Thermal Cycle at High Temperature—Test Series B

5.1 High Temperatures and Fire

The well-known mechanical behavior of concrete at high temperatures is largely unaffected by the type of concrete, whether ordinary or high-strength/high-performance, vibrated or self-compacting/consolidating, and regardless of whether siliceous, mixed or calcareous aggregates are used. There are, however, certain features that increase concrete's sensitivity to heat, leading to a greater reduction in mechanical properties and causing a more pronounced thermal spalling (Lo Monte et al., 2019 [44]). This is evident in mixes characterized by dense and homogeneous matrices, because of the addition of fillers, supplementary cementitious materials and/or high-range water reducers, as in HPCs. What is well established, however, is the sequence elastic modulus E_c/tensile strength f_t/compressive strength f_c, from the most to the least heat-affected parameter. In contrast, both the Poisson ratio ν_c and the fracture energy G_f increase with the temperature—up to 400°C–500°C and 300°C–400°C, respectively—under residual conditions, i.e., after cooling down to room temperature, before decreasing at higher temperatures. It should be noted that for $T < 200$°C, the previous sequence of E_c, f_t and f_c is less clear due to the expulsion of free water from the capillary pores, to the detriment of the compressive strength.

The complex behavior of concrete has unavoidable consequences for structural performance, particularly in concrete slabs subjected to punching, where all the aforementioned parameters come into play.

To advance understanding of the punching behavior of heat-damaged slabs, sixteen specimens were tested in residual conditions (T = 0°C, 105°C, 250°C, 400°C, Test Series B), with a focus on failure modes and truncated-cone formation.

5.2 Geometry of the Specimens, and Parameters under Investigation

Sixteen circular concrete slabs (eight unreinforced and eight net-reinforced) made of a high-performance concrete (f_c = 72 MPa) were cast and tested under punching loads in both virgin conditions and after a single thermal cycle. The external diameter, supported diameter, thickness, and loading-tip diameter are 440, 410, 75 and 30 mm, respectively (Figs. 2b and 3). The mix design (Table 1, Test Series B)—fairly typical of silica-fume *lean* concretes—has been used in Milan for several years in various structural applications. Since the aggregate is mostly crushed flint, this concrete is highly heat-sensitive (Felicetti and Gambarova, 2000 [5]). The eight reinforced specimens were provided with a net composed of deformed 6-mm bars spaced by 42 mm (reinforcement ratio close to 1% in each direction, Fig. 3b). The ramps of the thermal cycles (±0.2°C/min, controlled via the furnace thermocouple) were designed to guarantee *quasi-steady conditions* with minimal thermal gradients ($dT/dt \leq 0.2$°C/mm) and thermal stresses. During each thermal cycle, the *reference* temperature was maintained for 12 h. All specimens were pre-desiccated at 105°C for 7 days.

5.3 Test Set-up, Instrumentation, and Displacements

The test set-up was identical to that used in Test Series A (Fig. 2c). Each specimen was fastened to the cylindrical support by means of a steel ring (*clamping ring*), which in turn was blocked by ten levers (Fig. 3a), while in Test Series A only eight levers were used because the specimens were slightly smaller. Unlike Test Series A, no camera was used in Test Series B.

5.4 Results

Load-displacement response

Some of the load-displacement curves for both unreinforced and reinforced specimens are plotted in Fig. 9a,b, with each curve representing the average of two tests. Despite their higher peak load, or carrying capacity, (+50% in virgin conditions, and +20% after a cycle at 400°C, Fig. 10a)—RC slabs exhibit a much steeper softening branch compared to unreinforced slabs. However, they also display a higher residual strength (≈30% of the peak load in virgin conditions and >40% after the 400°C cycle) compared to 6%–12% in unreinforced slabs.

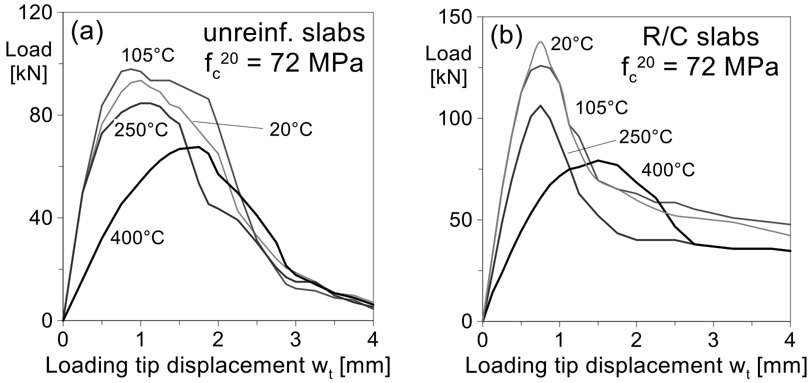

Figure 9: Curves of the load vs. the loading-tip displacement: (**a**) unreinforced specimens, Tests B0/1/2/3-C-H; and (**b**) RC specimens, Tests B0/1/2/3-N24-H.

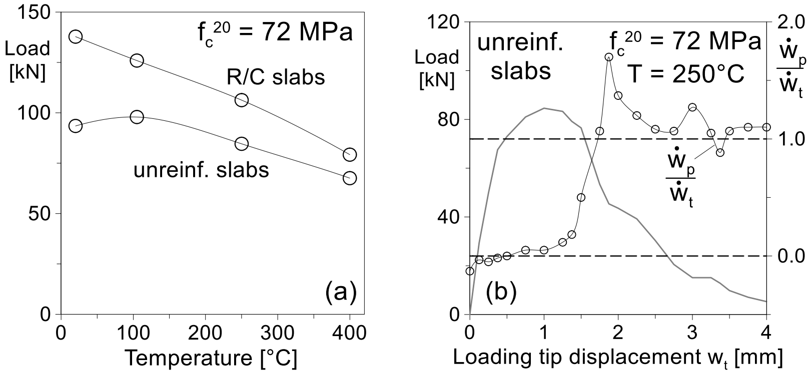

Figure 10: Strength and kinematic behavior of specimens Series B: (**a**) typical plots of the peak load vs. the temperature (Test B0/1/2/3-C-H and Test B0/1/2/3-N45-H); and (**b**) ratio of the punching-tip penetration rate to the loading-tip rate vs. the loading-tip displacement (Test B2-C-H).

In unreinforced slabs, most of the pre-peak nonlinearity arises from the formation and propagation of radial cracks at the intrados (*bending-type behavior*), while most of the post-peak softening is due to the interaction between the opening of the radial cracks and the formation and detachment of the truncated cone (*shear-type behavior*). This complex behavior is confirmed by the curves of the rate ratio $[(dw_p/dt)/(dw_t/dt)]$ vs. the loading-tip displacement w_t (Fig. 10b), whose peak past the maximum load—followed by an extended plateau—clearly indicates the formation and detachment of the truncated cone. It should be noted that for small values of w_t—when the slab behavior is mostly elastic—w_p (penetration of the punching tip) is negligible and the ratio $[(dw_p/dt)/(dw_t/dt)]$ is close to zero. For large values of w_t (namely after the formation of the punching cone), w_p tends to coincide with w_t and the previous ratio is close to—but slightly larger than—one, because of the recovery of the elastic deformation in the slab.

In RC slabs, the pre-peak linearity is relatively extended, because radial cracking is prevented or delayed by the reinforcement (Felicetti and Gambarova, 2000 [5]). Radial cracks start forming slightly before the stress peak and the activation of the punching cone. The combination of both crack types explains the steepness of the softening branch (Fig. 9b).

Owing to the restraining action of the reinforcement—which controls the opening of both radial cracks and the shear band associated with punching—the residual strength is greater, since the rough-cracked surfaces dissipate a significant amount of energy. Regarding the peak load (Fig. 10a), the slightly increasing trend observed in unreinforced slabs below 150°C is not found in RC slabs, whose peak load decreases almost linearly. RC slabs also appear to be slightly more heat-sensitive than unreinforced slabs. For example, after the cycle at 400°C, the normalized residual peak is slightly below 60% in RC slabs, but slightly above 70% in unreinforced slabs.

Displacements and cracking

The plots of the vertical displacement $\mathrm{w_i}$ measured at the intrados (Fig. 11, in three directions at 120°) clearly show that unreinforced specimens (Fig. 11a) exhibit bending-type behavior up to the stress peak, as demonstrated by the mostly linear diagrams consistent with the formation of radial cracks. The detachment of the truncated cone begins during the softening phase, between $F/F_{max} = 1$ and ≈ 0.75. In contrast, RC specimens (Fig. 11b) exhibit a more uniform distribution in the central zone, with an upward curvature starting from $F/F_{max} \approx 1$, indicating the activation of the truncated cone. In conclusion, RC slabs tend to exhibit a more pronounced shear-type behavior than unreinforced slabs.

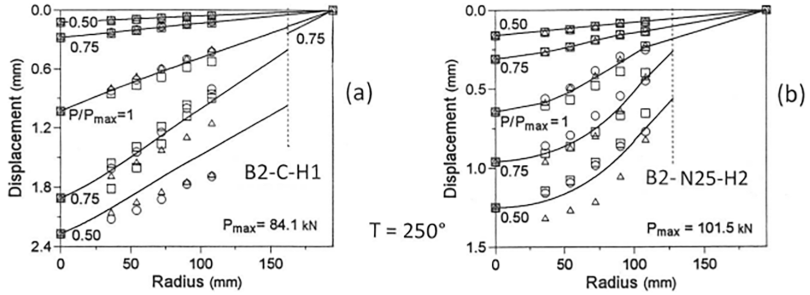

Figure 11: Vertical displacement at the intrados w_i, measured using the star-shaped support of Fig. 5a in three directions at 120°, and average diagrams (solid curves): (**a**) unreinforced, and (**b**) net-reinforced specimens.

In all tests, failure was characterized by the formation of a punching cone, preceded or accompanied by radial cracking. In unreinforced specimens, after removing the cone, the radial profiles of the fractured surface were plotted using a laser profile detector in 3 directions at 120° (Fig. 12a, Test B2-C-H1). In RC specimens, a cut was made using a diamond disk, at a right angle to the lower bar array (Fig. 12b, Tests B1/2/3-N25-H1/1/2).

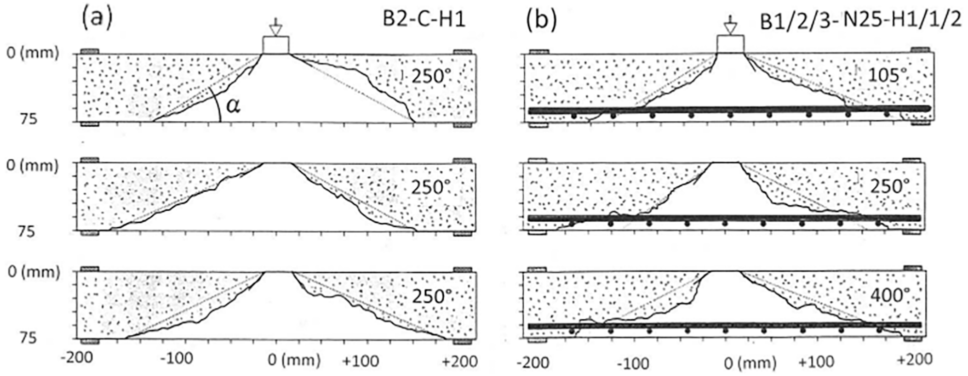

Figure 12: Typical profiles of the truncated-cone surface: (**a**) Test B2-C-H1 (unreinforced, T = 250°C) in 3 radial directions at 120°; and (**b**) Tests B1/2/3-N25-H1/1/2.

In unreinforced specimens, the average inclination α of the lateral surface of the cone was measured as indicated by the dotted lines in Fig. 12a (i.e., reference was made to the trace of the cone at the intrados of the specimen). In RC specimens, reference was made to the plane containing the centroids of the lower bars, to avoid the *skin effect* inside the cover, where the cracked surface tends to run horizontally toward the boundary.

In Fig. 13, the average values of the inclination α are plotted against the peak load for the 16 specimens. The effects of temperature and reinforcement are very limited. In unreinforced specimens α is slightly below 30° (29.4°), while in RC specimens it is slightly above 33° (33.2°). It should be noted that (a) each pair of connected points—starting from the right—refers to nominally-identical specimens tested under the same thermal conditions, and (b) the angle α is characterized by a more limited dispersion in unreinforced slabs (solid circles).

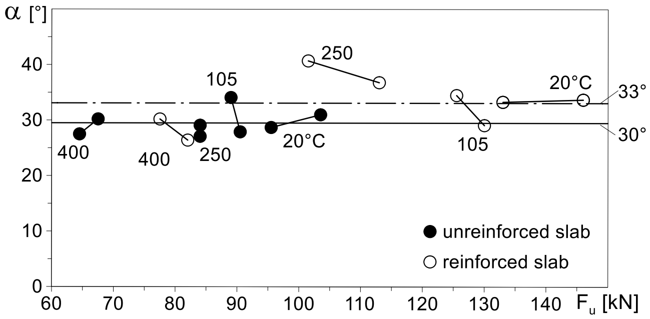

Figure 13: Average inclination α of the punching-cone surface with respect to the mean plane of the slab (Fig. 12), as a function of the ultimate load, for different temperatures; the average is approximately 30° in unreinforced specimens and close to 33° in net-reinforced specimens.

Returning to the displacements (see definitions in Section 4.2), Fig. 14a shows an example of an unreinforced specimen (Test B2-C-H1, after heating to 250°C), where the bending in plain-concrete specimens dominates up to the peak load. Punching only begins in the initial phase of softening and rapidly develops, while bending diminishes and local crushing plays a negligible role. As previously observed, the interaction between bending cracks and the punching cone dissipates energy, providing the specimen with a degree of ductility. Overall, the bending resistant mechanism characterizes the attainment of the peak load, while the large bending displacements during the softening phase foster the formation and detachment of the punching cone.

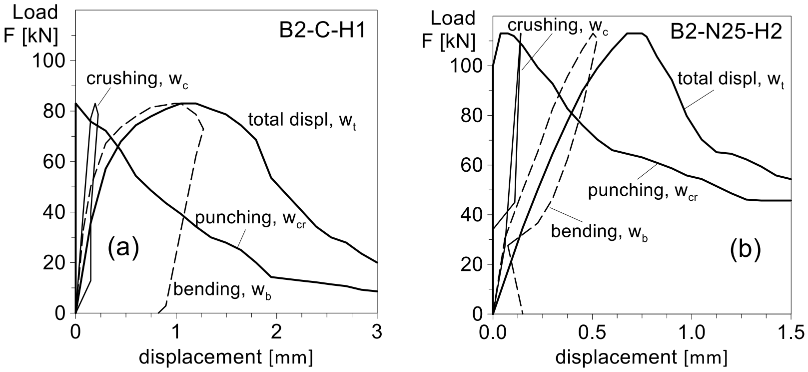

Figure 14: Displacement components: (**a**) unreinforced specimen (Test B2-C-H1); and (**b**) net-reinforced specimen (Test B2-N25-H2); both tests after a thermal cycle at 250°C, see Section 4.2.

In Fig. 14b, an example of a reinforced specimen (Test B2-N25-H2, after heating to 250°C) demonstrates that punching begins shortly before the peak load is reached, and that the coexistence of bending and punching during this phase makes softening much steeper. As bending rapidly diminishes during the softening phase, punching becomes the dominant resistant mechanism, while the contribution of crushing is even more limited than in unreinforced specimens. The reinforcement ensures a high residual capacity even at large punching displacements (1.5 mm at 40% of the peak load in Test B2-N25-H2), although part of this capacity can be attributed to the membrane behavior.

Overall, both bending and punching (the latter with a limited role) govern the attainment of the peak load. Soon after, the restraining action of the reinforcement limits the opening of radial cracks, making punching more abrupt yet more effective throughout the softening phase. Finally, both the reinforcement and thermal damage tend to shift the failure mode from bending to shear, with the detachment of a punching cone in both cases.

6 Fiber-Reinforced Slabs under Impulsive Punching—Test Series C

6.1 Loads

Concrete structures are often required to resist impact loads and shock waves, which may be caused by flying objects, fast-moving vehicles or major accidents like explosions, often followed by fire. These loads are typically applied over limited areas (as in punching), producing a multiaxial but localized state of stress and strain. Due to the high strain-rates associated with impact loading, *ad hoc* tests are necessary on concrete both with and without reinforcement or fibers, as well as on concrete structures. Among the latter, slabs subjected to punching have attracted the interest of many well-known scholars in the last decade of the twentieth century, including Bentur, Diotallevi, Krauthammer, Mindness, Naaman, Shah, Soroushian, Toutlemonde, Walraven, and Yankelevsky (see references in Gambarova and Schumm, 1994 [7]). More recent studies are also available, such as Zineddin and Krauthammer (2007) [45], Luccioni et al. (2017) [46], and Tuğrul Erdem (2021) [47]. The addition of steel fibers—as in many initial studies—and the increase of slab thickness enhance punching-shear performance, as shown by Yu et al. (2025) [48], using *machine learning*. Polymeric fibers with high elastic modulus are also attracting the interest of materials' experts (In acrylic fibers, the elastic modulus E_f = 14–25 GPa is close to E_c = 10–45 GPa commonly found in cementitious matrices).

In this third experimental campaign (Tests Series C), polyacrylonitrile fibers were used in concrete slabs subjected to punching under impact loading, with the focus on the role of the fibers in increasing energy dissipation and modifying the collapse mechanisms. The strain rate ranges from 10^{-4} to 10^{-2}, typical of low-speed impacts in Civil Engineering applications (speed of the striking object = 1–30 m/s). These conditions are consistent with previous studies, such as Zineddin and Krauthammer (2007) [45], where the speed of the punching tip is 2.5 m/s, very close to the value 2.85 m/s adopted in this work. As observed in the previous study, the lower the punching-tip speed (v_p)—and the larger the falling mass (M)—the more likely the occurrence of a bending-type failure (*global response*), while a higher speed and lower mass promote shear-type failure (*local response*). The speed adopted in this study ensures that both failure modes can occur, depending on fiber content.

Finally, as in the static case (Section 4 and Appendix B), the first cracks to appear are bending-related radial cracks at the intrados, which remain the only ones if the load does not reach the peak, see Wang et al. (2021) [49], who tested square net-reinforced slabs (side = 800 mm) under impact punching (side-to-thickness ratios 6.7–10.0; steel ratios 0.22%–0.40% in two directions; various positions of the impact point, and drop-hammer heights from 1.5 to 2.5 m). The hammer mass was relatively small (11.1 kg), and the impact speed was larger than in this study (5.4, 6.3, and 7.0 vs. 2.85 m/s).

6.2 Geometry of the Specimens, Test Setup, and Instrumentation

Forty-nine concrete specimens were cast in the form of square slabs, with the same dimensions as those tested in Test Series A (Fig. 2a). All specimens, except for the reference ones (made of plain concrete), contained polyacrylonitrile-PAN fibers. As in Test Series A—and with minor differences compared to Test Series B—the specimens were fastened to a cylindrical support using a steel *clamping ring*, which was in turn fixed by eight levers (Figs. 2b and 15a). As in Test Series B no camera was used; therefore, only the top sector of the cylindrical support of Tests Series A and B was employed (Fig. 15a). The diameter of the striking tip (30 mm), equal to that of the loading tip, has a hemispherical end and is 20% larger than the maximum aggregate size.

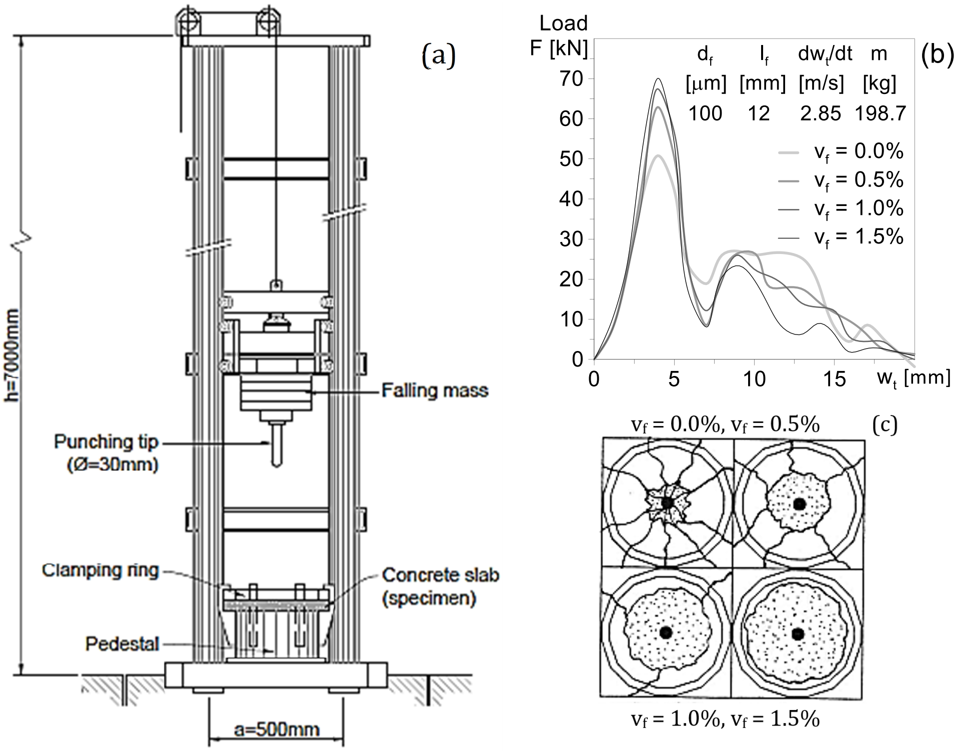

Figure 15: Details of the press and typical test results: (**a**) impact machine equipped with a falling-mass; (**b**) force-displacement curves for different fiber contents; and (**c**) failure modes and crack patterns in Tests C0-C-N and C0-P(1/2/3)21-N; PAN short fibers; aspect ratio λ_f = 120; m = falling mass.

The tests were performed using a falling-mass impact machine (Fig. 15a) equipped with an electric winch to lift the mass. The winch was released via an electromechanical control device. The main characteristics of the impact machine are listed below:

- Maximum falling mass and falling velocity M = 210 kg and v = 10.5 m/s;
- Maximum falling height h = 6.5 m;
- The falling mass is equipped with an accelerometer;
- Two photoelectric sensors, mounted on one of the columns, spaced 100 mm apart and placed close to the upper face of the specimen, allow the actual impact velocity to be evaluated by derivation;
- A displacement sensor monitors the instantaneous position of the falling mass, thereby providing an alternative means for evaluating the actual impact velocity;
- Acceleration, velocity and displacement of the falling mass are monitored at 100 μs intervals (10 kHz frequency) via a PC-based high-speed acquisition system.

In all tests, the actual mass and impact velocity were m = 199 kg and v = 2.85 m/s, respectively. Once the (negative) acceleration of the falling mass, including the striking tip, is known at each instant after contact with the slab, the total force acting on the falling mass—and thus on the slab—can be calculated. Since the total force applied to the slab is resisted partly through inertia and partly through the material's linear and nonlinear responses (with the latter dominating as the slab approaches failure), limiting the inertial effect makes it possible to obtain a clear understanding of the damage within the slab and on the resulting failure mode. These considerations support the choice of a relatively large falling mass and a relatively limited impact velocity, without compromising the dynamic nature of the tests. Well-established data, dating back to the last decade of the twentieth century (see Bentur and Mindness, 1990 [50]), indicate that both fibers and steel reinforcement reduce the influence of inertia forces.

The parameters investigated in this study are the fiber content (v_f = 0.0%, 0.5%, 1.0% and 1.5% by volume), their diameter (d_f = 40 and 100 μm) and their length (l_f = 12, 24 and 36 mm), resulting in four values of the aspect ratio (λ_f = 120, 360, 600, and 900). These define sixteen sub-cases, yielding a total of 48 specimens, since three nominally-identical specimens were tested for each sub-case (In one case a fourth specimen was tested, bringing the total to 49 specimens). All these tests are dynamic, since the *reference* static tests were conducted on the 22 + 4 specimens of Test Series A (with either PAN fibers or no fibers, see Table 1).

6.3 Results and Comments

The test results primarily consist of each specimen's response in terms of impact force vs. loading-tip displacement (Fig. 15b), with displacement measured relative to the slab's undeformed shape. The response curves are grouped according to the geometry of the fibers (diameter d_f, length l_f and aspect ratio $\lambda_f = l_f/d_f$) and the fiber content by volume (v_f). In addition to the response curves, the crack patterns and failure modes are a significant part of the results, as both clearly show that increasing fiber content shifts the failure mode from a mostly bending-related, *extended* failure to a predominantly shear-related, *localized* failure (Figs. 15c and 16, from left to right). For small or no fiber content, several radial cracks develop along the intrados of the slab (see also Gomathi et al., 2022 [51]) prior to the detachment of a relatively small truncated cone. In contrast, higher fiber contents lead to the formation of sizeable punching cones.

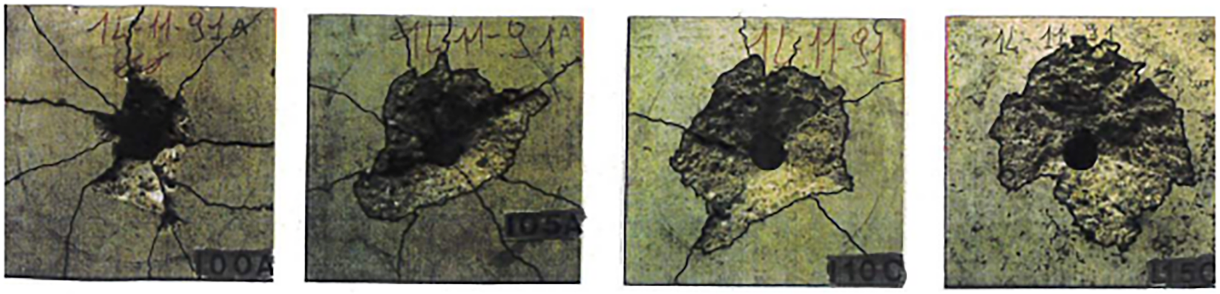

(a) C0-C-N2 (b) C0-P123-N1 (c) C0-P223-N1 (d) C0-P323-N2

Figure 16: Impulsive punching—typical failure modes for different fiber contents by volume: v_f = 0.0 (**a**), 0.5 (**b**), 1.0 (**c**) and 1.5% (**d**); fiber diameter, length and aspect ratio d_f = 100 μm, l_f = 36 mm (long fibers) and λ_f = 360; similar failure modes for all values of fiber diameter, length and aspect ratio.

Similar results were obtained at the end of the twentieth century by testing (a) circular slabs containing a steel net at the intrados and metallic fibers (static tests, Walraven et al., THIBO fibers, Delft, 1993 [10]), and (b) square slabs containing metallic hooked fibers subjected to a localized blast (0.5 and 1.0% by volume, Luccioni et al., 2017 [46]).

The examination of the failure mechanisms (Figs. 15c and 16) reveals (a) a slightly crushed zone originating at the extrados, followed by the formation of a cylindric hole (whose depth $\Delta s'$ is approximately 1/6 of the specimen thickness t, Fig. 17); (b) the detachment of a truncated cone (whose meridians—or directrices—can be represented by a three-linear curve, Fig. 17); and (c) the formation of radial cracks, which mainly propagate from the hole and extend into the concrete layers closest to the intrados. In the tests performed in this study, increasing the fiber content (from 0.0% to 1.5% by volume) results in the fractured surface of the truncated cone becoming more extended. At the same time, the number of the radial cracks decreases, regardless of the fiber aspect ratio (compare Figs. 15c and 16). Therefore, there are no clear indications that the fractured surface—and the dissipated energy—increases with the fiber content. It should be noted that the clamping ring (fixed to the cylindrical pedestal by eight levers) makes the boundary restraint relatively homogeneous, as shown by the densely-distributed radial cracks for $v_f = 0$, and the absence of radial cracks for $v_f = 1.5\%$ (Figs. 15c and 16d).

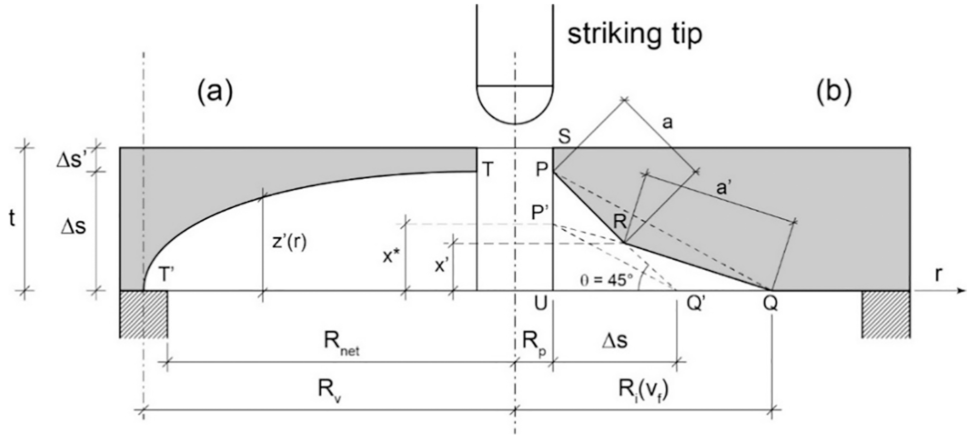

Figure 17: Crack profiles in radial planes: (**a**) bending cracks *TT'*; and (**b**) directrix *SPRQ* of the truncated cone; $P'Q'//PQ$; $\Delta s = 5/6\ t$; $\Delta s' = 1/6\ t$; $R_i = 3R_p$ for $v_f = 0$, and $R_i = R_{net}$ for $v_f = 1.5\%$ (from tests); $R_p = 15$ mm; $R_{net} = 145$ mm; thick full lines = profiles of cracked surfaces.

However, no circumferential cracks form at the extrados, along the ring. In other words, the clamping action along the boundary is limited, and so the negative bending moment in the radial planes. Typical force-displacement curves are plotted in Figs. 15b and 18, where two peaks appear (more in dynamic than in static tests). The first, and higher, is related to the *initial* behavior of the specimen, when the inertia of the largely undamaged specimen plays a significant role, together with concrete crushing beneath the punching tip, followed by the formation of radial cracks and the punching cone. The second, much lower, peak is associated with the activation of secondary post-failure resistant mechanisms. The two load peaks, as well as the energies dissipated during the formation of the crack system ($E_{stt}{}^*$ and $E_{dyn}{}^*$, Fig. 19c), and in the post-failure phase ($\Delta E_{stt} = E_{stt} - E_{stt}{}^*$, and $\Delta E_{dyn} = E_{dyn} - E_{dyn}{}^*$, Fig. 19a,b) are clearly introduced by Janabi and Esfahani (2025) [52], who performed static tests on RC slabs, with and without steel fibers and *integrity reinforcement* (top orthogonal bars placed inside the slab in the punching region, to guarantee structural integrity and stability in the post-failure phase).

Returning to the first peak, the activation of radial cracks shows that increasing the fiber content leads to a higher peak and a lower number of radial cracks, while the strength on cubes (not reported in this paper) is only marginally affected. However, the total dissipated energies (E_{dyn} and E_{stt} represented by the areas enveloped by the response curves in Fig. 18,) are not markedly and univocally influenced by fiber content, as shown by the tests performed under either static or dynamic conditions (Fig. 19a).

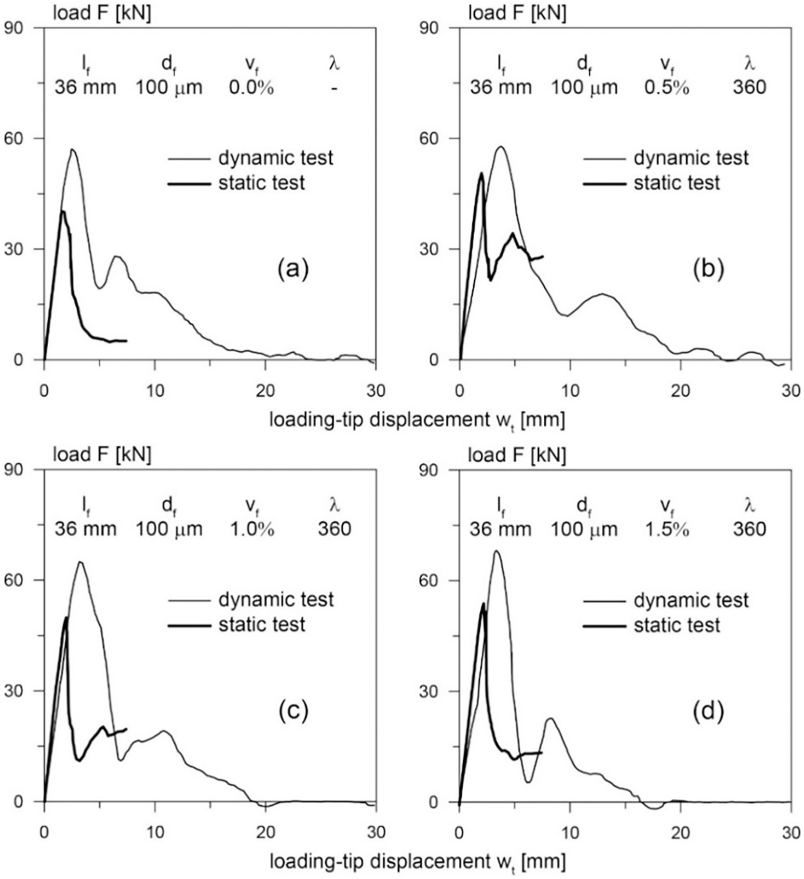

Figure 18: Load-displacement curves under static punching (Test Series A) and dynamic punching (Test Series C): (**a**) Specimen A0-C-N and C0-C-N; (**b**) A0-P123-N and C0-P123-N; (**c**) A0-P223-N and C0-P223-N; and (**d**) A0-P323-N and C0-P323-N.

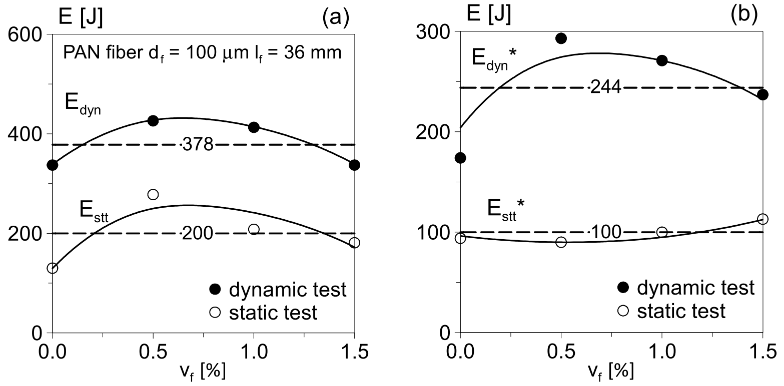

Figure 19: (Continued)

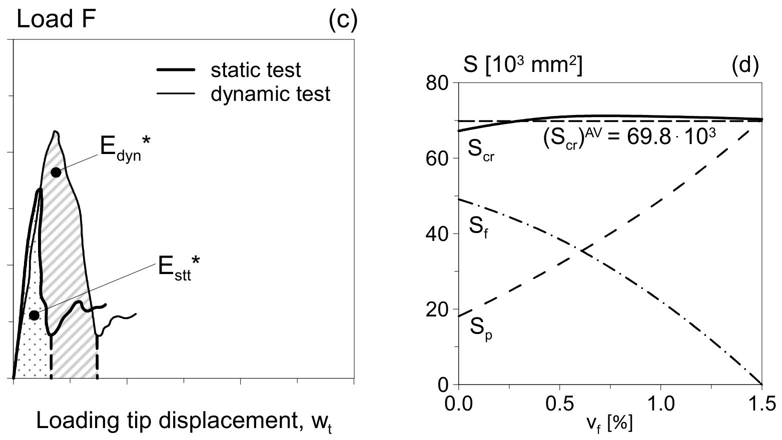

Figure 19: Energies and cracked surfaces vs. fiber content: (**a**) total dissipated energy under dynamic and static conditions (E_{dyn} and E_{stt}, respectively) from the tests in Fig. 18; (**b**,**c**) energies (E_{dyn}* and E_{stt}*) required by the formation of the crack system; and (**d**) cracked surfaces according to Eqs. (5) and (6), where S_{cr} = the total cracked surface; S_f = the total surface of the radial/bending cracks; and S_p = the lateral surface of the punching cone including the punching hole.

The same occurs for the energies dissipated during the formation of the punching cone and radial cracks (E_{dyn}* and E_{stt}*, Fig. 19b,c), where the areas enclosed by the response curves only include the first peak. A clear explanation is provided by the fractured surface S_{cr} (Fig. 19d) calculated using the simple model presented in Fig. 17. The two components S_p (lateral surfaces of the punching cone and the punching hole) and S_f (surface of the radial cracks) vary significantly since any increase in the fiber content results in a larger truncated cone but fewer radial cracks (Figs. 15c and 16). Nevertheless, the total fractured surface S_{cr} exhibits relatively small variation (Fig. 19d).

The model for evaluating the fractured surface is based on the following assumptions, which are valid only for the impulsive punching of PAN fiber-reinforced slabs (Fig. 17):

- The minimum radius of the truncated cone coincides with the radius R_p of the striking tip. At the top of the truncated cone a small cylinder forms (*punching hole*), whose depth Δ*s*' is assumed to be 1/6 t, where *t* is the thickness of the slab;
- The maximum radius R_i of the truncated cone is a linear function of the fiber content v_f;
- The directrix of the truncated cone is tri-linear, with the branch (PR) at 45° to the axis r;
- The line *P'Q'* connecting the intersections *P'* and *Q'* of the lines of the cracked sides with the reference axes is parallel to the line *PQ* connecting the points *P* and *Q*;
- The number of radial cracks n decreases with increasing fiber content v_f and represents the distribution of the radial cracks observed in the tests;
- The radial cracks extend to the entire nominal radius of the supported boundary R_v and their profile is described by a square-root function z' (r) of the radial distance *r*, whose maximum depth is equal to the depth Δ*s* of the truncated cone (Fig. 17).

The expressions of the various parameters are listed below:

$$R_i = 4.5 + 6.67v_f; \quad n = 9.5 - 3v_f - 2.22{v_f}^2 \text{where } R_i\,[\mathrm{cm}] \text{ and } v_f[\%] \tag{1}$$

$$x^* = \Delta s^2/(R_i - R_p); \quad x' = x^*[(R_i - R_p - \Delta s)/(R_i - R_p - x^*)] \tag{2}$$

$$a = (\Delta s - x')/\sin(45^\circ); \quad a' = \sqrt{x'^2 + (R_i - R_p - \Delta s + x')^2} \tag{3}$$

$$z'(r) = \Delta s \sqrt{(R_v - r)/(R_v - R_p)} \tag{4}$$

$$S_p = \pi \left[2R_p \Delta s' + (\Delta s - x')(a + a') + 2R_p a + (R_i + R_p) a' \right]; \quad S_f = 2/3 n R_v \Delta s \tag{5}$$

$$S_{cr} = S_p + S_f \tag{6}$$

In Eq. (1), $n = 9.5$ for $v_f = 0$ is the mean number of radial cracks observed in the tests, see for example—the crack patterns in Figs. 15c and 16.

6.4 Consistency of the Cracked Model with Available Values for Concrete Fracture Energy

To assess the consistency of the previous assumptions and expressions, reference is now made to the tests shown in Fig. 18 [4], whose energies E_{dyn} and E_{stt} (Fig. 19a, mean values 378 and 200 J, respectively) and $E_{dyn}{}^{*}$ and $E_{stt}{}^{*}$ (Fig. 19b,c, mean values 244 and 100 J, respectively) are used to evaluate the specific fracture energy of the concrete and to compare it with the values commonly found in the literature or provided by design codes.

For v_f = 0%, 0.5%, 1.0%, and 1.5%, the values of the fractured surface S_{cr} (Eqs. (5) and (6)) are 672, 705, 710, and 703 cm^2 (Fig. 19d). The mean value is $S_{cr}{}^{AV}$ = 698 cm^2.

Based on the two following assumptions:

- The energy dissipated inside the specimen under dynamic conditions is generally close to—or even less than—1/10 of the total dissipated energy; the values assumed here are 1/10 and 1/12, as indicated by Banthia, Bentur and Mindess in their works of the late eighties of the previous century.
- The energy dissipated in the fracture process—including the formation of large cone-shaped and radial cracks—is a fraction ($E_{dyn}{}^{*}$) of the total dissipated energy (E_{dyn}); the specific fracture energy $G_{f,test}$ resulting from the impact tests has the following mean value:

$$G_{f,test}{}^{AV} = (1/12 - 1/10)\, E_{dyn}{}^{*AV} / S_{cr}{}^{AV} = (0.083 - 0.100)\, 244/0.0698 = 291 - 349\ \mathrm{J/m^2} \tag{7}$$

The values obtained from Eq. (7) are consistent with the fracture energy of plain concrete under static direct tension, as reported in the CEB Model Code 90 (1990):

$$G_f = 0.2\,(10 + 1.25 d_a)\, f_c{}^{0.7} = 120\ \mathrm{J/m^2} \tag{8}$$

where f_c = 46 MPa and the maximum aggregate size d_a = 25 mm, provided that: (a) the mixed nature of fracture in concrete punching, including cracking in tension and shear, as well as friction, is accounted for by increasing G_f (+30% is a commonly accepted rough approximation); and (b) the difference between the energy dissipated under dynamic and static conditions is considered, as under dynamic conditions the dissipated energy may even more than double, as shown in Fig. 19a,b:

$$G_{f,dyn}{}^{AV} = 1.3 \cdot 2 \cdot G_f = 319\ \mathrm{J/m^2} \tag{9}$$

It is noteworthy that the value provided by Eq. (9) not only falls between the values provided by Eq. (7), but practically coincides with their mean value (320 J/m^2). It should also be noted that: (a) Eq. (8) was preferred over other, more recent expressions for its straightforwardness, as it clearly and directly incorporates aggregate size and concrete tensile strength, but not fiber content—an acceptable limitation for PAN fibers; (b) the limited dependence of dissipated energy on fiber content and geometry in the case of PAN fibers ($E_{dyn}{}^{AV}$ = 378 J, Fig. 19a, fiber length = 36 mm) is confirmed by the tests cited in Fig. 15c

(E_{dyn}^{AV} = 420 J, fiber length 12 mm); and (c) the limited effect of PAN fibers can be explained by the small variability of the total cracked surface S_{cr} with fiber content v_f (Fig. 19d).

With regard to the last point, however, it should be noted that whether S_{cr} is roughly constant or exhibits a downward/upward concavity as a function of fiber content depends on the variability of the number n of radial cracks, as larger values of n result in a larger downward concavity, while smaller values of n produce a greater upward concavity. Overall, the generally larger downward concavity exhibited by the plots of the energies (Fig. 19a,b, except for E_{stt}*) with respect to the downward concavity of the plot of the total cracked surface (Fig. 19d) may be due to different cracking modes, as Mode 2 (dominant in the formation of the punching cone) tends to dissipate more energy than Mode 1 (dominant in the formation of radial cracks).

7 Conclusions

Static and dynamic tests on unreinforced, fiber-reinforced, and net-reinforced concrete slabs representing the region around a localized load clearly show that punching remains a brittle phenomenon. The post-peak strength loss varies depending on the fiber and reinforcement content, as well as on the damage induced by high temperatures. As a rule, a larger reinforcement content corresponds to greater structural ductility and residual strength in the post-failure phase. Polyacrylonitrile fibers, however, are considerably less effective than either steel hooked fibers or steel nets, at similar volumes (1%–2%). In fact, the static tests at room temperature conducted in this research show that the residual strength in the softening phase are close to 15%–30% of the peak load with PAN fibers, compared to 40% for steel hooked fibers and to 65%–70% for steel nets. The type of failure—shear-bending failure with radial cracking or punching-shear failure with cone-shaped cracking—can be identified during testing by measuring and comparing the displacements at the intrados and extrados of the slab. In fact, fairly homogeneous displacements in the central part of the intrados indicate the formation of a punching cone, provided that displacements at the extrados are limited or even negligible. Controlling the displacement of the punching-tip is essential as snap-back phenomena may occur during the transition phase from pre-peak bending-type behavior to post-peak shear-type behavior.

The static tests on the slabs pre-heated up to 105°C, 250°C and 400°C—although limited to a single specimen geometry, one concrete grade (a high-performance, highly-siliceous concrete), and one reinforcement ratio (in addition to the specimens made of plain concrete)—reveal some interesting trends: (a) the strength decreases sharply above 100°C (−15% to −20% at 250°C), while ductility increases above 250°C, in both reinforced and unreinforced specimens; (b) although characterized by the formation of a punching cone in the post-peak phase, unreinforced slabs exhibit clear bending-type behavior at low to medium temperatures ($T \le 250$°C), with a tendency towards shear-type behavior at higher temperatures ($T > 250$°C); (c) reinforced-concrete slabs are more shear-sensitive at all temperatures, as shown by their steeper softening branch accompanying the formation of the punching cone; and (d) at higher temperatures, the contribution of reinforcement to slab bearing capacity in punching decreases, due to the shift towards shear-type failures. In the tests performed in this study, the bearing capacity of unreinforced slabs is approximately two-thirds that of reinforced slabs at room temperature, but exceeds 85% after heating to 400°C. In static tests, the peak of the load-displacement response is always accompanied by the formation of radial cracks of varying extent at the intrados, while the post-peak behavior is clearly characterized by the formation of a punching cone, responsible for a sudden strength loss.

Regarding the impact behavior, polyacrylonitrile fibers increase the peak load under dynamic punching, as is well-known for steel fibers and high-modulus polymeric fibers. This increase—approximately + 25% for fiber contents between 0.5% and 1.5% by volume—is primarily attributed to the high strain-rate sensitivity of fiber-concrete interface. The failure mode under dynamic punching is greatly affected by fiber content, as low fiber contents lead to mixed-mode failures in bending and shear, with the formation of radial cracks at the intrados and a localized punching cone. Conversely, at high fiber contents, radial cracks tend to disappear and the punching cone dominates. In the tests performed in this study, no radial cracks were observed at a fiber content of 1.5% by volume. Fiber content, however, has a limited and ambiguous effect on the total energy dissipated during the impact and subsequent perforation. Nevertheless, the energy dissipated through the formation and detachment of the punching cone increases with fiber content, while the energy dissipated through the formation of radial cracks decreases. The density of the radial cracks remains a key parameter in the evolution of fractured surfaces with fiber content. In fact, the total fractured surface may exhibit a relative maximum or minimum as fiber content increases, depending on the bending-shear interaction and the density of the radial cracks, as shown in this study.

Overall, the behavior of moderately thick concrete slabs subjected to punching—representing the hogging regions of larger slabs—remains a challenge. Each investigation, however, helps clarify specific aspects. In this study, for example, the shift towards more shear–controlled failure mechanisms because of fiber content, heat, and impact provides new, partly-unexpected insights, that may contribute to safer structural design.

Acknowledgement: The authors wish to acknowledge the in-kind contributions by the firm MONTEFIBRE Ltd. (Milan, Italy) for providing the materials (fibers and additives for the concrete) and by the Department of Aeronautical Engineering (now Aerospace Engineering) of the Politecnico di Milano, which made available the impact machine for the dynamic tests. Special thanks are due to Professor Patrick Bamonte (DICA, Politecnico di Milano) for his valuable suggestions and comments.

Funding Statement: The authors received no specific funding for this study.

Author Contributions: Roberto Felicetti: investigation, methodology, data curation (high-temperature tests); Pietro G. Gambarova: conceptualization, investigation, data curation (impact tests), writing (original draft), supervision; Francesco Lo Monte: data curation (static tests), interpreting of the results, writing (review and editing). All authors reviewed and approved the final version of the manuscript.

Availability of Data and Materials: The data and the materials are available in a few dedicated references, as well as in several MS and PhD open-access dissertations placed in the library of the Politecnico di Milano or made available by the authors on demand.

Ethics Approval: Not applicable.

Conflicts of Interest: The authors declare no conflicts of interest.

Appendix A Labeling of the Specimens

Specimens' labelling: XT-Yfdl-Zq

Test Series A and C: T = 20°C; Test Series B: T = 20, 105, 250 and 400°C

Test Series (n. of tests)	Specimen	$f \rightarrow v_f$ [%]				$d \rightarrow d_f$ [μm], d_s [mm]					$l \rightarrow l_f$ [mm]		
		1	2	3	4	1	2	3	4	5	1	2	3
A(34) f_c = 43 MPa or 46 MPa	A0-C-N1/2 (*) (**)	.	.	.	.	.	.	.	.	.	.	.	.
	A0-Pfdl-N1/2 (**)	0.5	1.0	1.5	.	30	100	.	.	.	12	24	36

(Continued)

(continued)

Test Series (n. of tests)	Specimen	f → v_f [%]				d → d_f [μm], d_s [mm]					l → l_f [mm]		
		1	2	3	4	1	2	3	4	5	1	2	3
	A0-Sfdl-N1/2 (*)	.	1.0	1.5	.	.	.	500	.	.	.	.	30
	A0-Nfd-N1/2 (*)	.	$1.0^{\wedge}$	.	$2.0^{\wedge\wedge}$	.	.	.	5	6	.	.	.
B(16) f_c = 72 MPa	B0/1/2/3-C-H1/2	.	.	.	.	.	.	.	.	.	.	.	.
	B0/1/2/3-Nfd-H1/2	.	.	.	$2.0^{\wedge\wedge\wedge}$	.	.	.	.	6	.	.	.
C(49) f_c = 46 MPa	C0-C-N1/2/3	.	.	.	.	.	.	.	.	.	.	.	.
	C0-Pfdl-N1/2/3	0.5	1.0	1.5	.	30	100	.	.	.	12	24	36

Note 1: f_c = 43 MPa in (*), and 46 MPa in (**). **Note 2:** two-way nets with ∅5 bars spaced by 65 mm (ˆ), ∅6 bars spaced by 47 mm (ˆˆ) and ∅6 bars spaced by 42 mm (ˆˆˆ); *d, d_s* = fiber, bar diameter; l_f = fiber length. **Note 3**: for each of the 51 sub-cases, roughly two tests were performed (99 tests), with 1–2 tests in each sub-case of Test Series A, 2 tests in each sub-case of Test Series B and 2–3 tests in each sub-case of Test Series C.

In Test Series A, the 34 specimens were subdivided into 5 sub-series:

- 18 specimens (first sub-series) containing polyacrylonitrile fibers (PAN fibers) with v_f (content by volume) = 0.5%, 1.0%, 1.5%, length l_f = 12, 24, 36 mm, diameter d_f = 30, 100 μm;
- 2 × 2 specimens (second sub-series, to check test repeatability) as in the previous sub-series (PAN fibers) with v_f = 1.0%, 1.5%, diameter d_f = 100 μm, length l_f = 12 mm;
- 2 × 2 specimens (third sub-series) containing hooked steel fibers (DRAMIX) with v_f = 1.0%, 1.5%, length l_f = 30 mm, diameter d_f = 500 μm;
- 4 specimens (fourth sub-series) containing a steel net with reinforcement ratios (in each direction) p_x = p_y = 0.5% + 0.5%, 1.0% + 1.0%, bar diameter/bar spacing 5/65 mm and 6/47 mm;
- 4 specimens (fifth sub-series): 2 specimens with f_c = 43 MPa and 2 specimens with f_c = 46 MPa; all specimens made of plain concrete (*reference* specimens).

Appendix B Specimens Reinforced with PAN Fibers and Steel Nets

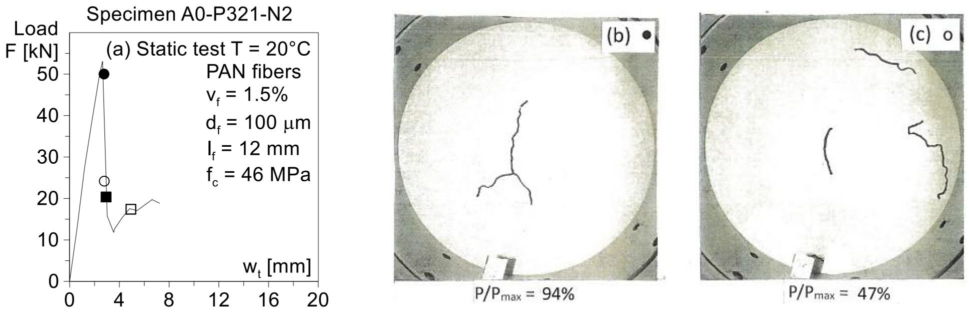

Figure A1: (Continued)

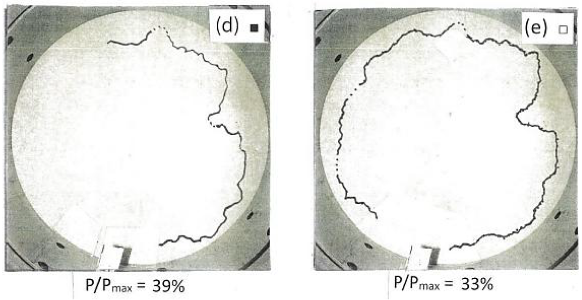

Figure A1: Quasi-static punching—PAN fibers (v_f = 1.5%): (**a**) load vs. loading-tip displacement; (**b**) first bending-controlled microcracks; (**c**) from radial to circumferential shear-controlled cracking; (**d**) partial development of the truncated cone; and (**e**) full development of the truncated cone.

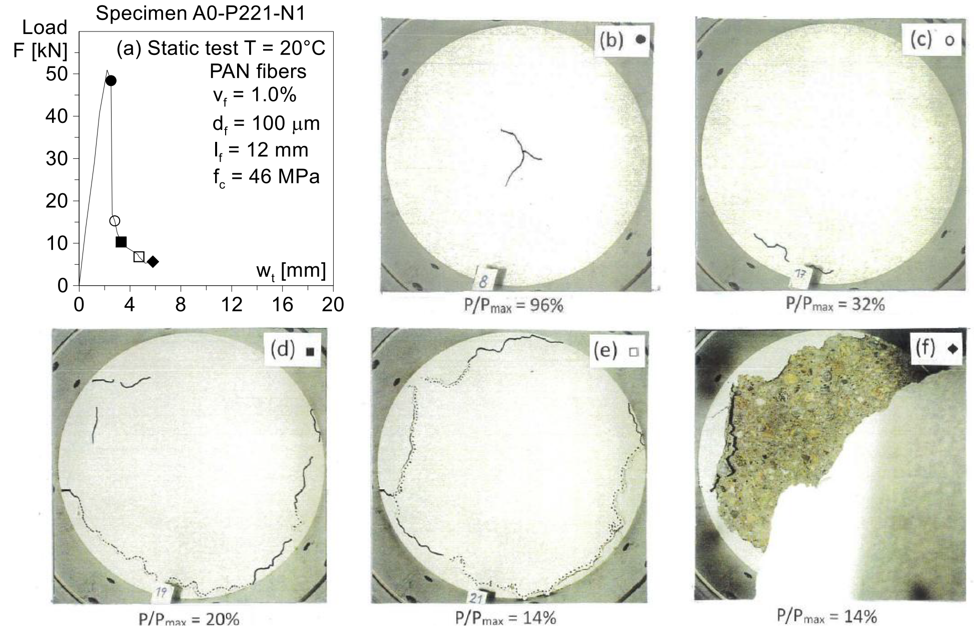

Figure A2: Quasi-static punching—PAN fibers (v_f = 1.0%): (**a**) load vs. loading-tip displacement; (**b**) first bending-controlled microcracks; (**c**) from radial to circumferential shear-controlled cracking; (**d**) partial development of the truncated cone; (**e**) full development of the truncated cone; and (**f**) detachment.

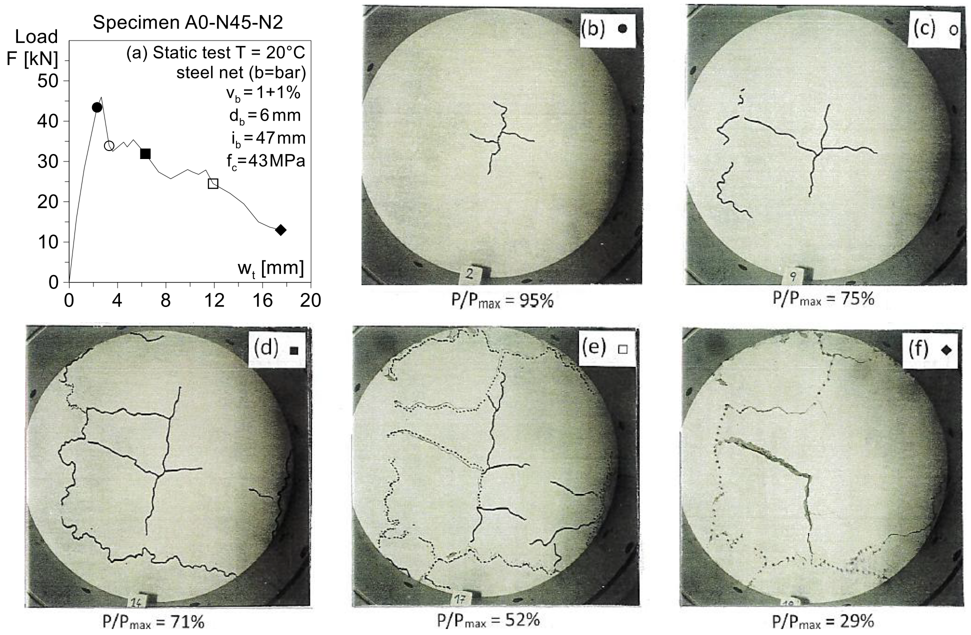

Figure A3: Quasi-static punching—Steel net: (**a**) load vs. loading-tip displacement; (**b**) first bending-controlled microcracks; (**c**) from radial to circumferential shear-controlled cracking; (**d**) partial development of the truncated cone; (**e**) full development of the truncated cone; and (**f**) detachment of the truncated cone.

Appendix C Test Reliability

As observed in Section 4.2 for Test Series A, a full statistical analysis of the results is not feasible since the number of specimens tested in each sub-case was limited (≤3). However, some indications of test reliability can be obtained by comparing the force-displacement responses of nominally-identical specimens.

For Test Series B, two examples are shown in Fig. A4, both after heating to 250°C; the first illustrates a pair of unreinforced specimens (Fig. A4a), and the second a pair of net-reinforced specimens (Fig. A4b).

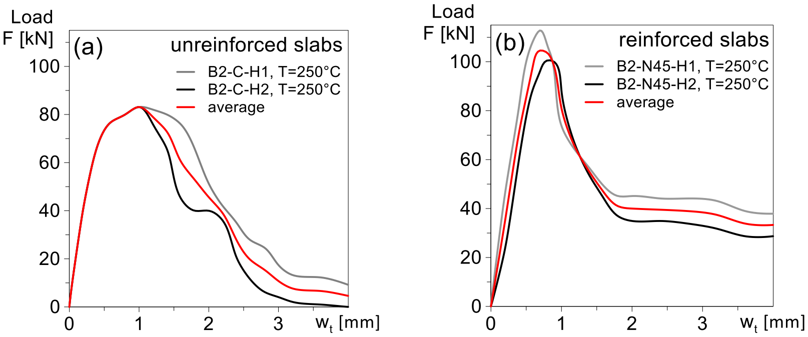

Figure A4: Static punching of thermally-damaged specimens—Test Series B: Load vs. loading-tip displacement curves; steel net in Specimens B2-N45-H1/2 (v_s = 1 + 1%); mean response curves in red; f_c = 72 MPa.

In general, the repeatability of the tests improves with increasing temperature, because heat-induced damage tends to be uniformly distributed, provided that the concrete mass is slowly heated and cooled. In this way, thermal gradients are minimized, as was done in all high-temperature tests conducted in this study. Fig. A4 indicates that test repeatability is acceptable. Test reliability is, therefore, confirmed.

For Test series C, an example is shown in Fig. A5a,b,c, where the response curves of three identical specimens reinforced with PAN fibers are plotted side-by-side. Also in dynamic conditions, test repeatability is more than acceptable, as a confirmation of test reliability. In addition, the results indicate that the higher the fiber content, the less dispersed the mechanical properties of the material, to the advantage of test reliability.

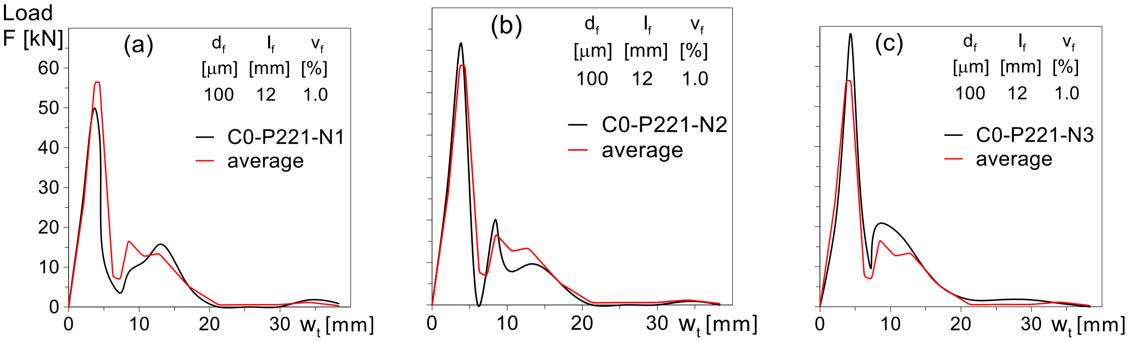

Figure A5: Dynamic punching of PAN fiber-reinforced specimens—Test series C: load vs. loading-tip displacement curves; PAN fibers; mean response curve in red; f_c = 46 MPa.

References

1. CEB Bulletin No. 168. Punching shear in reinforced concrete: a state-of-art report. Lausanne, Switzerland: Secrétariat permanent, Comité euro-international du béton; 1985.
2. fib Bulletin No. 12. Punching of structural concrete slabs. Lausanne, Switzerland: fib Fédération internationale du béton; 2001.
3. Venkata Ramana N. Review on punching shear strength of slabs. Int J Eng Res Dev. 2017;13(10):1–25. doi:10.14359/51738758.
4. Felicetti R, Gambarova PG, Zanini N. On crack propagation and failure modes in fiber-reinforced concrete slabs. In: Proceedings of Fracture Mechanics for Concrete and Concrete Structures (FraMCoS-2); 1995 Jul 25–28; Zurich, Switzerland. p. 813–22.
5. Felicetti R, Gambarova PG. On the residual behavior of HPC slabs subjected to high temperatures. In: Proceedings of the PCI/FHWA/FIB International Symposium on High Performance Concrete Precast/Prestressed Concrete; Federal Highway Administration and Federation Internationale du Beton; 2000 Sep 25–27; Orlando, FL, USA. p. 598–607.
6. Guastini C, Bartoli G, di Prisco M. Tests on influence of aging time on punching shear strength of HPFRC circular slabs. In: Proceedings of the fib Symposium on Engineering a Concrete Future: Technology, Modeling and Construction; 2013 Apr 22–24; Tel-Aviv, Israel. p. 365–8.
7. Gambarova PG, Schumm C. Impulsive punching of fiber-reinforced concrete slabs. In: Proceedings of the Structures Congress XII; 1994 Apr 24–28; Atlanta, GA, USA. p. 252–7.
8. fib Bulletin No. 57. Shear and punching shear in RC and FRC elements. Salò, Italy: fib fédération internationale du béton; 2010.
9. Ospina CE, Mitchell D, Muttoni A. Punching shear of structural concrete slabs—Honoring Neil M. Hawkins. Lausanne, Switzerland: fib fédération internationale du béton; 2016.
10. Walraven JC, Pat MGM, Markov I. The punching shear resistance of fibre-reinforced concrete slabs. Delft, The Netherlands: Delft University of Technology, Stevin Laboratory; 1993.
11. Zamri NF, Mohamed RN, Awalluddin D, Abdullah R. Experimental evaluation on punching shear resistance of steel fibre reinforced self-compacting concrete flat slabs. J Build Eng. 2022;52:104441. doi:10.1016/j.jobe.2022.104441.
12. Liu J, Chen B, Afefy HM, Sennah K. Experimental study on punching shear behavior of ultra-high-performance concrete (UHPC) slabs. Buildings. 2025;15(10):1656. doi:10.3390/buildings15101656.

13. Sucharda O, Smirakova M, Vaskova J, Mateckova P, Kubosek J, Cajka R. Punching shear failure of concrete ground supported slab. Int J Concr Struct Mater. 2018;12(1):36. doi:10.1186/s40069-018-0263-6.
14. Bassurucu M, Turk K, Turgut P. The effect of hybrid fiber and shear stud on the punching performance of flat-slab systems. J Build Eng. 2023;77:107555. doi:10.1016/j.jobe.2023.107555.
15. Hernández Fraile D, Faccin E, Minelli F, Plizzari G, Muttoni A. Fibre orientation in SFRC slabs and consequences for punching shear and flexural resistance. Eng Struct. 2024;302:117364. doi:10.1016/j.engstruct.2023.117364.
16. Nguyen-Minh L, Rovňák M, Tran-Quoc T, Nguyenkim K. Punching shear resistance of steel fiber reinforced concrete flat slabs. Procedia Eng. 2011;14(4):1830–7. doi:10.1016/j.proeng.2011.07.230.
17. Mabrouk RTS, Hegab AA. Analysis of the punching behavior of RC flat slabs with horizontal and vertical shear reinforcement. In: Proceedings of the International Conference on Advances in Sustainable Construction Materials & Civil Engineering Systems (ASCMCES-17). Les Ulis, France: EDP Sciences; 2017.
18. Bentz EC, Netopilik RJ. Test results of punching shear on 500 mm thick reinforced concrete slabs. In: Proceedings of the fib Symposium on Engineering a Concrete Future: Technology, Modeling and Construction; 2013; Apr 22–24; Tel-Aviv, Israel. p. 269–272.
19. Trekin N, Pekin D. Experimental research on punching shear mechanisms in reinforced concrete slabs. In: Proceedings of the XXII International Scientific Conference “Construction the Formation of Living Environment” (FORM-2019); 2019 Apr 22–24; Moscow, Russia. 12 p.
20. De Sousa AMD, Lantsoght EO, El Debs MK. Transition between shear and punching in reinforced concrete slabs: review and predictions with ACI code expressions. ACI Struct J. 2023;120(2):115–28. doi:10.14359/51738350.
21. Marí A, Spinella N, Rodríguez MF. Mechanical model for the shear-punching strength of steel fiber reinforced concrete slabs under concentric loading. Structures. 2023;52(1):854–67. doi:10.1016/j.istruc.2023.04.035.
22. Said M, Mahmoud AA, Salah A. Performance of reinforced concrete slabs under punching loads. Mater Struct. 2020;53(4):68. doi:10.1617/s11527-020-01509-5.
23. Schmidt P, Kueres D, Hegger J. Punching shear behavior of reinforced concrete flat slabs with a varying amount of shear reinforcement. Struct Concr. 2020;21(1):235–46. doi:10.1002/suco.201900017.
24. Bashandy AA, Mohamed FA, Arab MA, Elkassas AI. Resisting punching shear of flat slabs. Int J Adv Res Sci Eng Technol. 2022;9(2):19019.
25. Awad R, Al Ateyat A, Junaid MT, Al-Sadoon Z, Altoubat S, Maalej M, et al. Punching shear capacity of fiber-reinforced concrete suspended slabs: database analysis and models assessments. J Build Eng. 2024;83(5):108433. doi:10.1016/j.jobe.2023.108433.
26. Hamoda A, Abadel AA, Ahmed M, Wang V, Vrcelj Z, Liang QQ. Punching shear performance of reinforced concrete slab-to-steel column connections incorporating ECC and UHPECC. Eng Struct. 2025;322(8):119145. doi:10.1016/j.engstruct.2024.119145.
27. Daud RA, Daud S, Al-Allaf MH, Alrshoudi F. Behaviour of slabs under impact loading: a review. Al Nahrain J Eng Sci. 2025;28(1):129–37. doi:10.29194/njes.28010129.
28. Bamonte P, Felicetti R, Gambarova PG. Punching shear in fire-damaged reinforced concrete slabs. ACI Spec Publ. 2009;265:345–66. doi:10.14359/51663303.
29. Bamonte P, Fernandez Ruiz M, Muttoni A. Punching shear strength of R/C slabs subjected to fire. In: Proceedings of the 7th International Conference on Structures in Fire (SiF 2012); 2016 Jun 6–8; Zurich, Switzerland. p. 689–698.
30. Ghoreishi M, Bagchi A, Sultan M. Review of the punching shear behavior of concrete flat slabs in ambient and elevated temperature. J Struct Fire Eng. 2013;4(4):259–80. doi:10.1260/2040-2317.4.4.259.
31. Ghoreishi M, Bagchi A, Sultan MA. Punching shear behavior of concrete flat slabs in elevated temperature and fire. Adv Struct Eng. 2015;18(5):659–74. doi:10.1260/1369-4332.18.5.659.
32. Annerel E, Lu L, Taerwe L. Punching shear tests on flat concrete slabs exposed to fire. Fire Saf J. 2013;57:83–95. doi:10.1016/j.firesaf.2012.10.013.
33. Smith HKM. Punching shear of flat reinforced-concrete slabs under fire conditions [dissertation]. Edinburgh, UK: University of Edinburgh; 2016.
34. Ožbolt J, Ruta D, İrhan B. Impact analysis of thermally pre-damaged reinforced concrete slabs: verification of the 3D FE model. Int J Impact Eng. 2019;133:103343. doi:10.1016/j.ijimpeng.2019.103343.

35. Hoang LC, Pop A. Punching shear capacity of reinforced concrete slabs with headed shear studs. Mag Concr Res. 2016;68(3):118–26. doi:10.1680/macr.15.00033.
36. Biyan B, Sharma A, Fetwi E, Ozbolt J. A new predictive equation for punching shear strength of reinforced concrete flat slabs based on numerical parametric study. Eur J Mater Sci Eng. 2023;8(3):156–82. doi:10.36868/ejmse.2023.08.03.156.
37. Huang C, Ma Q, Pu S. Comparative analysis of punching shear strength for reinforced concrete slabs based on database. In: Proceedings of the 2016 International Conference on Innovative Material Science and Technology (IMST 2016); 2016 Aug 19–21; Shenzhen, China. p. 467–71. doi:10.2991/imst-16.2016.69.
38. dos Santos JB, Muttoni A, de Melo GS. Enhancement of the punching shear verification of slabs with openings. Struct Concr. 2023;24(2):3021–38. doi:10.1002/suco.202200714.
39. Muttoni A, Fernández Ruiz M. The Critical Shear Crack Theory as a mechanical model for punching shear design and its application to code provisions. fib Bulletin. 2010;57:31–60. doi:10.35789/fib.bull.0057.ch03.
40. EN 1992-1-1:2023. Eurocode 2-design of concrete structures part 1-1: general rules and rules for buildings, bridges and civil engineering structures. Brussels, Brussels: CEN-CENELEC Management Centre; 2003.
41. Dönmez A, Bažant ZP. Size effect on punching strength of reinforced concrete slabs with and without shear reinforcement. ACI Struct J. 2017;114(4):875. doi:10.14359/51689719.
42. Timoshenko SP, Woinowsky-Krieger S. Theory of plates and shells. 3rd ed. New York, NY, USA: McGraw Hill; 1987.
43. Bažant ZP, Cao Z. Size effect in punching shear failure of slabs. ACI Struct J. 1987;84(1):44–53. doi:10.14359/2785.
44. Lo Monte F, Felicetti R, Rossino C. Fire spalling sensitivity of high-performanceconcrete in heated slabs under biaxial compressive loading. Mater Struct. 2019;52(1):14. doi:10.1617/s11527-019-1318-0.
45. Zineddin M, Krauthammer T. Dynamic response and behavior of reinforced concrete slabs under impact loading. Int J Impact Eng. 2007;34(9):1517–34. doi:10.1016/j.ijimpeng.2006.10.012.
46. Luccioni B, Isla F, Codina R, Ambrosini D, Zerbino R, Giaccio G, et al. Effect of steel fibers on static and blast response of high strength concrete. Int J Impact Eng. 2017;107(6):23–37. doi:10.1016/j.ijimpeng.2017.04.027.
47. Tuğrul Erdem R. Dynamic responses of reinforced concrete slabs under sudden impact loading. J Constr. 2021;20(2):346–58. doi:10.7764/rdlc.20.2.346.
48. Yu X, Khodadadi N, Song A, Yu Y, Nanni A. Prediction and analysis of punching shear capacity in steel fiber reinforced concrete slab using machine learning. Results Eng. 2025;27(8):105646. doi:10.1016/j.rineng.2025.105646.
49. Wang Y, Liu J, Xiao Z, Zhao F, Cheng Y. Experiment and simulation study on the dynamic response of RC slab under impact loading. Shock Vib. 2021;2021(1):7127793. doi:10.1155/2021/7127793.
50. Bentur A, Mindess S. Fibre reinforced cementitious composites. London, UK: Elsevier Applied Science; 1990.
51. Gomathi KA, Rajagopal A, Prakash SS. Predicting the failure mechanism of RC slabs under combined blast and impact loading. Theor Appl Fract Mech. 2022;119(14):103357. doi:10.1016/j.tafmec.2022.103357.
52. Janabi A, Esfahani MR. Enhancing punching shear and post-punching behavior of flat slabs using wire mesh, integrity bars and fibers. Sci Rep. 2025;15(1):33911. doi:10.1038/s41598-025-09552-4.